# On the In Situ Cyclic Resistance of Natural Sand and Silt Deposits

Armin W. Stuedlein, M.ASCE[1]; Amalesh Jana[2]; Ali Dadashiserej[3]; and Xiao Yang, M.ASCE[4]

**Abstract:** This study presents cyclic resistances of an instrumented medium dense sand (i.e., the Sand Array) and medium plastic silt (i.e., the Silt Array) deposit deduced from in situ dynamic testing using the controlled blasting test method. Particle velocity records were used to calculate the cyclic resistance ratios, *CRR*s, and convert the transient blast-induced ground motions into their equivalent number of shear stress cycles, $N_{eq}$, through consideration of the cyclic resistance observed from stress-controlled, constant–volume, cyclic direct simple shear (DSS) tests. The $CRR$-$N_{eq}$ relationship developed for the medium dense sand deposit demonstrated that the in situ cyclic resistance is larger than that (1) expected from cyclic DSS test specimens reconstituted to the in situ vertical effective stress, relative density, and shear wave velocity, $V_s$; and (2) calculated using case history-based, penetration-, and $V_s$-based deterministic formulations of liquefaction triggering models. Differences between the in situ cyclic resistance and that computed using probabilistic liquefaction triggering models reduced somewhat when considering probabilities of liquefaction exceeding 50% and 85%, depending on the model. Partial drainage during dynamic loading of the Sand Array appears to have contributed to the cyclic resistance of the sand deposit, with an increase of 6% to 27% compared to that estimated for fully undrained conditions. Differences between the cyclic failure criteria used to interpret the cyclic resistance of intact laboratory specimens of silt result in significantly different interpretations of the in situ *CRR*; the use of maximum excess pore pressure-consistent criteria appears to provide the best representation of the in situ, stress-based cyclic resistance when high quality, intact silt specimens form the basis for conversion of transient seismic waveforms to uniform shear stress loading cycles. The investigation described herein suggests that the reduction of cyclic resistance for plastic soils to account for multidirectional shaking ranges from 0% to 7% over $N_{eq}$ of 1 to 100. **DOI: 10.1061/JGGEFK.GTENG-10784.**

## Introduction

The complexity of soil liquefaction or cyclic softening during an earthquake arises from the interaction of transient, highly irregular multidirectional loading, spatial variability, redistribution of excess pore pressures, and the in situ system response of stratified soil deposits (Abdoun et al. 2013; Dobry and Abdoun 2015a, b; Cubrinovski et al. 2019). Many other factors such as particle shape, soil fabric, fines content, plasticity, relative density, aging, cementation, stress history, and prestraining contribute to the complexity of liquefaction triggering and cyclic softening (Seed and Lee 1965; Finn et al. 1970; Mulilis et al. 1975; Ladd 1977, 1978; Seed 1979; Dobry et al. 1982; Chang et al. 1982; Troncoso and Verdugo 1985; Koester 1994; Singh 1994; Sanin and Wijewickreme 2006; Dobry and Abdoun 2015a; El-Sekelly et al. 2016, 2017; Dahl et al. 2014, 2018; Wijewickreme et al. 2019). Many studies have noted the challenges associated with laboratory testing, which include the replication of the desired soil fabric, dynamic loadings, and drainage conditions that exist in the field. Nonetheless, efforts to sample and test soils in undisturbed states have revealed pertinent findings (e.g., Yoshimi et al. 1984, 1989; Lee et al. 2012; Ishihara et al. 2016; Esposito and Andrus 2017; Beyzaei et al. 2018; Wijewickreme et al. 2019; Jana and Stuedlein 2021b). However, sampling soils in an intact, relatively undisturbed state is difficult, particularly for clean and silty sands, gravels, and larger materials, and the true in situ drainage conditions may not be well-simulated in the laboratory (Dobry and Abdoun 2015b; Cubrinovski et al. 2019). Thus, various empirical, case history-based liquefaction triggering relationships relying on in situ penetration resistance (Seed et al. 1985; Youd and Idriss 2001; Moss et al. 2006; Cetin et al. 2018; Boulanger and Idriss 2014) and small strain shear wave velocity, $V_s$ (Andrus and Stokoe 2000; Kayen et al. 2013) have been developed and widely adopted in practice. The accuracy of these relationships is inferred following earthquakes based on evidence of liquefaction observed at the ground surface (e.g., Cubrinovski et al. 2010; Ashford et al. 2011; Franke et al. 2019), consistent with the liquefaction/no liquefaction cases on which these models were developed. However, liquefaction in the absence of surface manifestation point to the potential error introduced when system responses prevent surface expression of liquefaction (Upadhyaya et al. 2022). The actual in situ cyclic resistance mobilized during earthquake loading is generally unknown with the exception, perhaps, of the insights drawn from the Wildlife Array (Zeghal and Elgamal 1994; Zeghal et al. 1995).

Controlled blasting provides an in situ testing technique that has been implemented in medium stiff silt and medium dense sand deposits at depths as great as 25 m below the ground surface (Jana et al. 2021; Jana and Stuedlein 2021a, 2022). However, the results of these and other in situ test programs (e.g., vibroseis shaking;

---

[1]Professor, School of Civil and Construction Engineering, Oregon State Univ., 101 Kearney Hall, Corvallis, OR 97331. ORCID: https://orcid.org/0000-0002-6265-9906

[2]Postdoctoral Researcher, School of Civil and Construction Engineering, Oregon State Univ., 101 Kearney Hall, Corvallis, OR 97331 (corresponding author). ORCID: https://orcid.org/0000-0003-1130-4037. Email: janaa@oregonstate.edu

[3]Graduate Research Assistant, School of Civil and Construction Engineering, Oregon State Univ., 101 Kearney Hall, Corvallis, OR 97331.

[4]Professor, School of Civil Engineering, Chongqing Univ., Chongqing 400045, China. ORCID: https://orcid.org/0000-0002-9411-4660

Note. This manuscript was submitted on February 7, 2022; approved on October 25, 2022; published online on February 9, 2023. Discussion period open until July 9, 2023; separate discussions must be submitted for individual papers. This paper is part of the ***Journal of Geotechnical and Geoenvironmental Engineering***, © ASCE, ISSN 1090-0241.

J. Geotech. Geoenviron. Eng., 2023, 149(4): 04023015

Roberts et al. 2016; Jana et al. 2022) have been largely interpreted within the cyclic strain approach developed by Dobry et al. (1982). In contrast, the more widely implemented simplified methods used for liquefaction triggering and cyclic softening evaluations rely on the cyclic stress approach. This study presents a methodology to quantify the in situ dynamic shear stresses mobilized within the moderately deep silt and deep sand deposits previously described by Jana and Stuedlein (2021a, 2022) and the interpretation of cyclic resistance using the cyclic stress approach. The cyclic resistance and its variation with the equivalent number of uniform loading cycles for the sand deposit is then compared to the results of specimens reconstituted to the same relative density, shear wave velocity, and vertical effective stress as that in the field, whereas the cyclic resistance of the silt deposit is compared directly to that obtained from cyclic direct simple shear tests on intact specimens. The relative accuracy of in situ penetration (SPT, CPT) and $V_s$ test-based liquefaction triggering models is investigated for the sand deposit and the influence of the assumed logarithmic slope of the cyclic resistance ratio curve, natural soil fabric, and partial drainage is discussed. This paper demonstrates the utility of the controlled blasting dynamic test methodology for the in situ evaluation of the cyclic resistance of any soil deposit at any depth of interest.

## Site and Subsurface Conditions

The test site is located on properties owned and operated by the Port of Portland and the relevant subsurface conditions have been described in detail by Jana and Stuedlein (2021a, 2022); relevant conditions are briefly reviewed herein. Several controlled blasting test programs were performed using a linear array of casings [Fig. 1(a)] to accommodate explosive charges and boreholes for the placement of instruments forming the Sand and Silt Arrays, including triaxial geophone packages (TGPs) and pore pressure transducers [PPTs; Fig. 1(b)]. The centers of the Sand and Silt Arrays are located at depths of 25 and 10.2 m, respectively.

In situ subsurface explorations included cone penetration tests (CPTs), standard penetration tests (SPTs) with energy measurements, vane shear tests (VSTs), and downhole geophysical tests

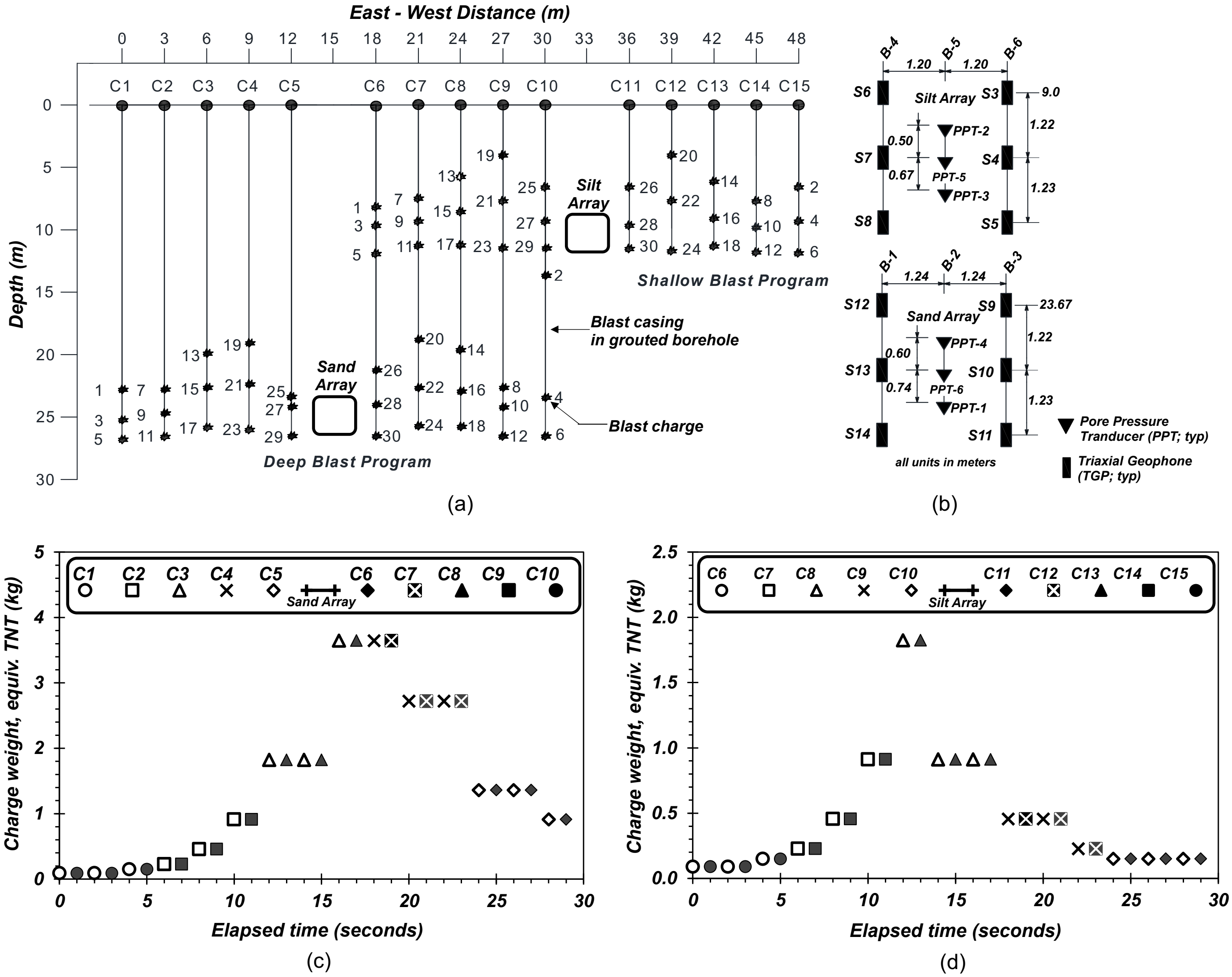

**Fig. 1.** In situ experimental program: (a) elevation view of the blast array, aligned due East and West, showing the location and detonation sequence of each charge for two blast events; (b) elevation view of the Silt and Sand Arrays; (c) 30 s detonation sequences comprising the Deep Blast Program (adapted from Jana and Stuedlein 2021a); and (d) shallow blast program (reproduced with permission from Jana and Stuedlein 2022).

to develop the geotechnical model of the subsurface (Jana and Stuedlein 2021a, 2022). Dredge sand and silty sand fill extends from the ground surface to a depth 5 to 6 m and is underlain by an approximately 2-m-thick layer of recent, native, alluvial, loose, clean sand. Below the native sand deposit lies a 5-to-6-m-thick alluvial, medium stiff, clayey silt (ML and MH) deposit with occasional partings of sandy silt (ML). Extending below the silt layer and to the depth of the explorations lies a deep deposit of alluvial, medium dense, clean sand (SP) to sand with silt (SP-SM). The deposits studied herein are relatively young Holocene deposits (Evarts et al. 2009). The depth of the groundwater table varied from approximately 3 to 7.3 m due to seasonal fluctuation of the nearby Columbia River and groundwater pumping operations over the course of this study. The depth of the water table was 4.2 m, with initial hydrostatic and nonhydrostatic pore pressures observed within the Silt and Sand Arrays, respectively, during the in situ tests described herein. The effective stresses used for the interpretation of all in situ test data were computed using the pore pressures measured during the corresponding explorations and dynamic tests.

The average plasticity index, $PI$, of the silt deposit is 28, and the overconsolidation ratio, $OCR$, varies from 1.6 to 2.2. The soil behavior type indices, $I_c$ (Robertson 2009) and corrected cone tip resistance, $q_t$, varies from 2.9 to 3.1 and 0.82 to 1.15 MPa, with averages of 2.99 and 0.95 MPa, respectively, over the depths of 8.89 m to 11.45 m within the Silt Array. The measured, initial average $V_s$ of intact natural silt specimens consolidated to their in situ stresses was approximately 122 m/s, similar to that obtained using in situ downhole tests (Donaldson 2019). Over the depths of the Sand Array, the material is characterized as medium dense, poorly graded fine sand (SP) and sand with silt (SP-SM), with fines content, $FC$, varying from 3.9% to 12.1% and 6% on average. The $I_c$ varies from 1.79 to 2.22 and is 1.9 on average. The overburden stress corrected, equivalent clean sand cone tip resistance, $q_{c1Ncs}$, varies from 83 to 108, with an average $q_{c1Ncs}$ of 98, and overburden stress, energy-, and clean sand-corrected SPT blow count, $N_{1,60cs}$, varies from 13 to 17, with an average $N_{1,60cs}$ of 15, over the instrumented depths of the Sand Array (n.b., $q_{c1Ncs}$ and $N_{1,60cs}$ were calculated using Boulanger and Idriss 2014).

## Stress-Controlled Cyclic Direct Simple Shear Response

Boulanger and Idriss (2015) describe the influence of the exponent, $b$, describing the power law relationship between the cyclic resistance ratio, $CRR$, and the number of uniform loading cycles, $N$, on the magnitude scaling factor, $MSF$, and equivalent number of cycles, $N_{eq}$. As described below, exponent $b$ controls the conversion of transient dynamic loadings to $N_{eq}$. Cyclic direct simple shear (DSS) tests were therefore conducted to facilitate the conversion of blast-induced ground motions to equivalent uniform loading cycles and were supplemented by CPT-based estimates of $b$ for the Sand Array due to the use of reconstituted sand specimens.

### *Laboratory Response of Reconstituted Sand Specimens*

Stress-controlled, constant–volume, cyclic DSS tests were performed on reconstituted sand specimens using materials collected from split-spoon samples. The typical height and diameter of sand specimens were 20 and 72 mm, respectively, which were air-pluviated into membrane-lined DSS rings and consolidated to the in situ vertical effective stress $\sigma'_{vc} = \sigma'_{v0} = 240$ kPa to achieve the in situ $V_s = 218$ m/s (measured using bender elements) and estimated relative density, $D_r = 51\%$ (Jana 2021). Specimens were subjected to varying amplitudes of uniform, sinusoidal loading with cyclic stress ratios, $CSR = \tau_{cyc}/\sigma'_{vc}$ using a frequency of 0.1 Hz. Individual stress-strain hysteresis and stress paths are presented in Jana (2021). Fig. 2(a) presents the variation of $CSR$ with the number of cycles required to reach a typically used cyclic failure criterion of a single amplitude shear strain, $\gamma_{SA} = 3\%$ (Ishihara and Yoshimine 1992; Boulanger and Seed 1995; Boulanger and Idriss 2007; Idriss and Boulanger 2008; Dahl et al. 2014; Price et al. 2017; Tasiopoulou et al. 2020), and which may be described using a power law (Idriss and Boulanger 2008; Xiao et al. 2018)

$$CRR = a \cdot N^{-b} \tag{1}$$

where $a = 0.20$ and $b = 0.125$ corresponding to the fitted coefficient and exponent, respectively. Fig. 2(a) also presents the $CRR$–$N$ relationship for the $N$ corresponding to the maximum excess pore pressure ratio, defined as the ratio of excess pore pressure, $u_e$ and $\sigma'_{vc}$, $r_{u,max} = 72\%$, corresponding to the in situ $r_{u,max}$ observed

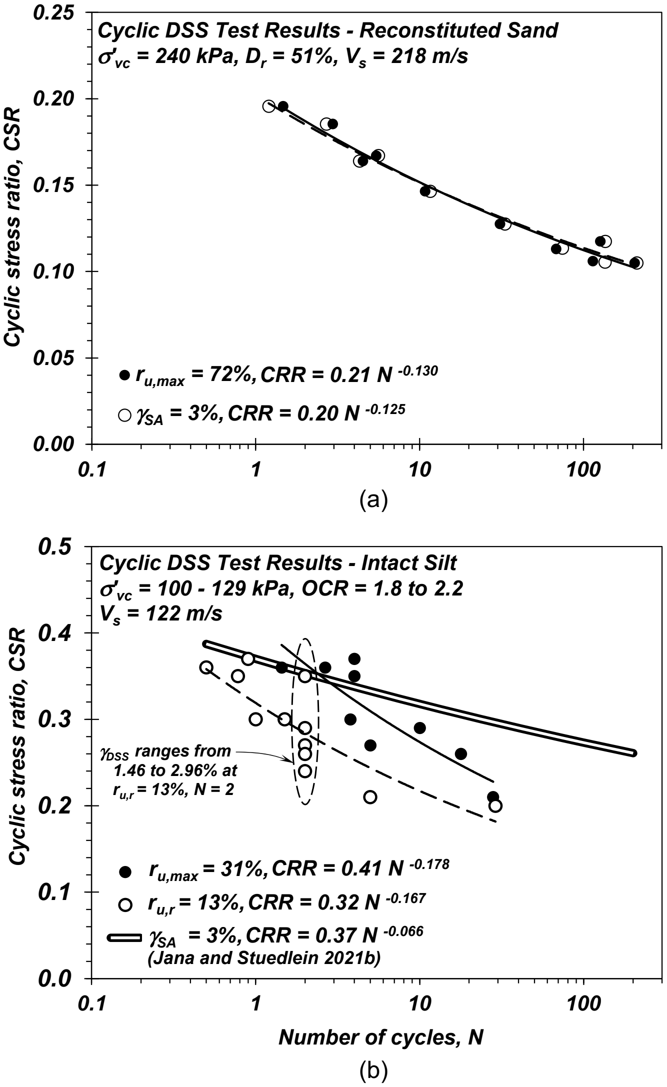

**Fig. 2.** Cyclic stress ratio versus number of uniform loading cycles corresponding to a single amplitude shear strain of 3% and various excess pore pressure ratios observed in situ: (a) reconstituted sand; and (b) intact silt specimens.

in the Sand Array. The similarity between the two cyclic failure criteria is evident.

### *Laboratory Response of Intact, Natural Silt Specimens*

Thin-walled tube samples were retrieved from the silt deposit during the installation of instruments and transported to the laboratories at Oregon State University for testing. Assessment of sample quality, stress history, monotonic undrained shear strength, and cyclic responses are reported by Jana and Stuedlein (2021b). Intact specimens were consolidated to the in situ $\sigma'_{vc}$ of ∼106 kPa prior to shearing under constant-volume, stress-, and strain-controlled loadings. Fig. 2(b) presents the variation of *CSR* with $N$ to reach $\gamma_{SA} = 3\%$ for quantification of exponent $b$ and comparison to the in situ cyclic resistance of the silt deposit, described below. The power law [Eq. (1)] describing the *CRR*-*N* curve is characterized by $a = 0.369$ and $b = 0.066$ (Jana and Stuedlein 2021b). Fig. 2(b) also presents the variation of *CRR* with $N$ to reach $r_{u,max} = 31\%$ and residual excess pore pressure ratio, $r_{u,r} = 13\%$ (corresponding to $r_u$ at the end of a given loading cycle) for comparison to the in situ cyclic resistance of the silt deposit under similar conditions, as described below. Under *CSR*s ranging from 0.24 to 0.35, the maximum shear strain, $\gamma_{DSS,max}$ ranged from 1.46 to 2.96% in the cycle corresponding to $r_{u,r} = 13\%$, and appears to suggest relatively poor correlation between stress-based *CSR*, $N$, and $\gamma_{DSS}$. In contrast, the strain-based relationship between $r_{u,r}$, $N$, and $\gamma_{DSS}$ was observed to be clear (Jana and Stuedlein 2021b) as noted by others (e.g., Dobry and Abdoun 2015b). The exponents corresponding to the two $r_u$-based *CRR*-*N* criteria are more than twice as large as that using the $\gamma_{SA} = 3\%$ cyclic failure criterion, and serves to impact the interpreted in situ cyclic resistance of the silt, as described below.

## In Situ Dynamic Tests Executed

Fig. 1(b) presents the elevation view of the instruments forming the Sand and Silt Arrays which were deployed to capture the in situ dynamic response at the corresponding depths. Each array required two boreholes to place the 28 Hz TGPs and one borehole to place PPTs. Additional instruments, not described herein for brevity, were installed within a fourth borehole; refer to Jana et al. (2021) for a full discussion of the calibration and deployment of each instrument. The arrays formed two rectangular elements each, termed Elements 1 and 2, and facilitated the deduction of shear modulus, shear strain, and excess pore pressure relationships using the finite element methodology (Rathje et al. 2001; Chang et al. 2007; Cox et al. 2009; Sahadewa et al. 2015; Roberts et al. 2016; Jana et al. 2021). In the Sand Array, Element 1 is formed by TGPs S10, S11, S13, and S14, whereas Element 2 is formed by TGPs S9, S10, S12, and S13. In the Silt Array, Element 1 is formed by TGPs S3, S4, S6, and S7, whereas Element 2 is formed by TGPs S4, S5, S7, and S8. Each TGP functioned as a node in its corresponding element, where integrated particle velocities facilitated calculation of blast-induced shear strains in the sand and silt deposits (Jana and Stuedlein 2021a, 2022).

Controlled blasting was performed in three separate blasting events: the Test Blast Program, the Deep Blast Program, and the Shallow Blast Program. The Test Blast Program was performed to evaluate ground motion attenuation, assess data acquisition, and to measure small strain crosshole shear wave velocities in the Silt and Sand Arrays. The primary objective of the Deep and Shallow Blast Programs was to dynamically excite the soils within the Sand and Silt Arrays, respectively, although the instruments comprising each array were monitored during each blast program. Refer to Jana et al. (2021) and Jana and Stuedlein (2021a, 2022) for details related to these three distinct test programs, dynamic responses including the relationships between excess pore pressure generation and shear modulus reduction with shear strain, and changes to the soil fabric following the blast programs. Fig. 1(a) presents the position and detonation sequence of the charges for the Deep and Shallow Blast Programs. During the Test Blast Program, charges were placed within a single casing CX [not shown in Fig. 1(a)], located 30 m west of casing C1. Charges were placed in casings C1 through C10 for the Deep Blast Program, whereas charges were housed in casings C6 through C15 for the Shallow Blast Program. Figs. 1(c and d) present the detonation sequence for the Deep and Shallow Blast Programs, conducted using 1 s delays. Charges were detonated sequentially on either side of the arrays to reverse the polarity of maximum shear strains and shear stresses. For brevity, this study focuses on the response of the Sand Array during the Deep Blast Program and that of the Silt Array during the Shallow Blast Program.

## Characterization of Blast-Induced Ground Motions

The main assumptions necessary to compute dynamic shear stresses from blast-induced ground motions concerns the dimensionality of the motion at the scale of interest and the relevance of $P$-waves. Figs. 3(a and g) present example longitudinal ($x$) and vertical ($z$; transverse) particle velocity time histories measured in TGP S13 of the Sand Array during the Deep Blast Program and TGP S8 of the Silt Array during the Shallow Blast Program, respectively. In both blast programs, the amplitudes of particle velocities were initially small, due to the small charges deployed and relatively large ray path distances. The amplitudes increased gradually, exhibiting the desired polarity reversal due to the alternating azimuthal bearings of the ray paths. The blast programs concluded with amplitudes of 2.083 and 0.505 m/s for the Deep and Shallow Blast Programs, respectively. Figs. 3(b–f and h–l) compare the body wave amplitudes and phases of various transverse waveforms measured in vertically adjacent TGPs S12 and S13 (Borehole B-1) and TGPs S7 and S8 (Borehole B-4) during the Deep [Fig. 1(c)] and Shallow Blast Programs [Fig. 1(d)], respectively. These waveforms illustrate the arrival of the high frequency $P$-wave, followed by the low frequency near- and far-field shear waves ($SV$-waves). Critically, the amplitude and phase of the $SV$-waves measured 1.2 m apart are nearly identical for most of the detonations, indicating near-planar shear wave fields within each element at the scale of the measurements. Slight differences in ray path distances between the sources and the instruments, and variability in soil properties and local diameter of the grout columns encapsulating the TGPs, produce small differences between the $SV$-wave amplitudes and phases, which may be neglected. However, the charges closest to the Sand Array (e.g., Blasts #26 through #30) exhibited larger differences in phase and amplitude, indicative of three-dimensional (3D) wavefields. It is assumed below that all blast-induced ground motions can be represented by two-dimensional (2D) wavefields for the purposes of computing shear stresses.

The normalized Fourier spectra for 30 individual particle velocity records recorded using TGP S14z during the Deep Blast Program and TGP S6z during the Shallow Blast Program, the corresponding averages, and the average for all TGPs are presented in Figs. S1(a and c). The average Fourier spectra of the full waveforms [Figs. S1(b and d)] indicate that the predominant frequency of motion recorded in the Sand and Silt Arrays are 13.4 and 14.6 Hz, respectively. The Stockwell spectrograms for example waveforms presented in Figs. S2(c and g)indicate average $P$-wave frequencies of 1,185 and 187 Hz in the Sand and Silt Arrays, respectively. The $P$-wave frequency in the silt deposit is lower than that in the sand

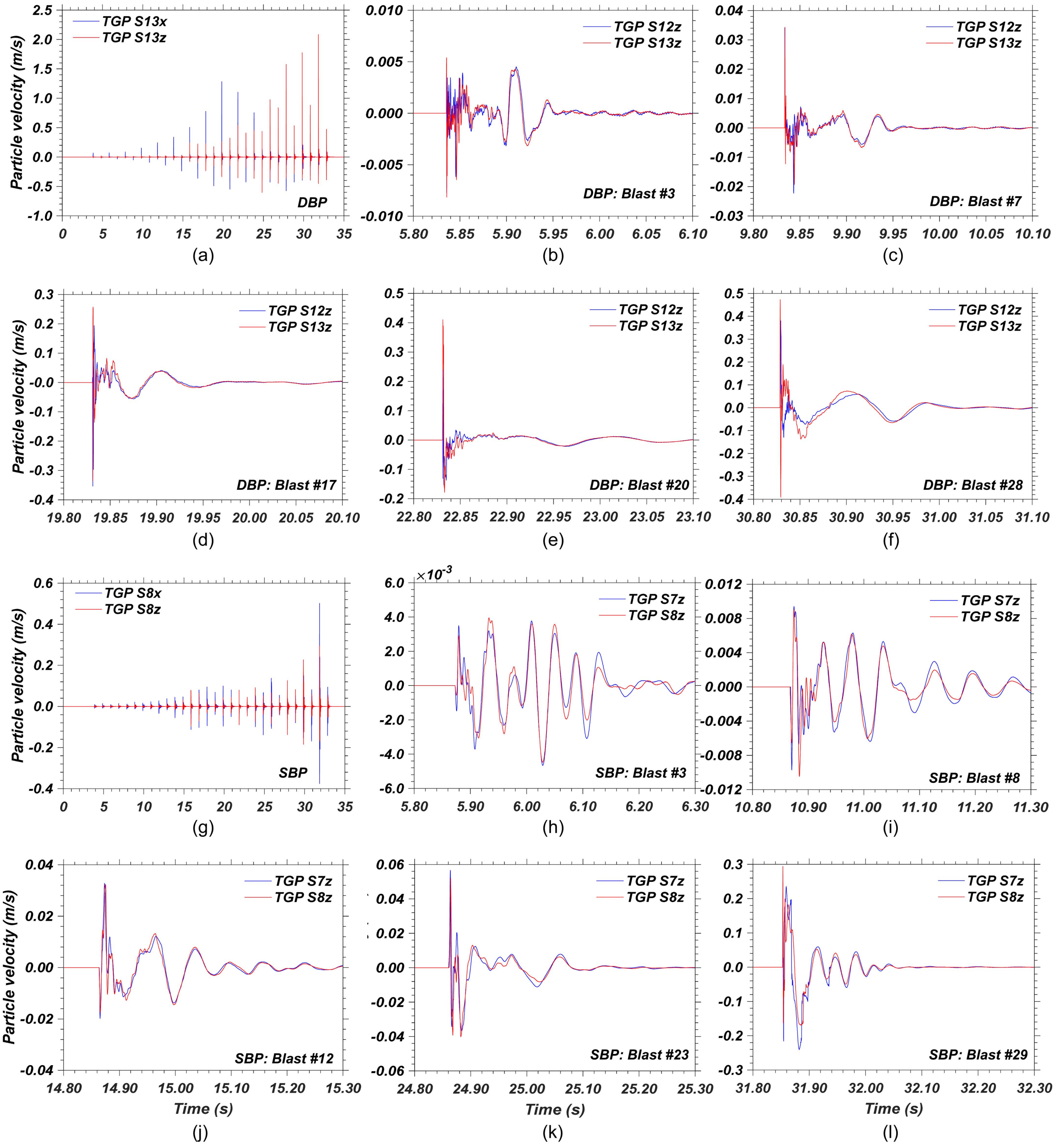

**Fig. 3.** Ground motions recorded in the Sand and Silt Arrays: (a) 30 s particle velocity time history at TGP S13, and comparison of the body waves and phases for vertically separated TGPs S12 and S13 located within Borehole B-1 for the (b) Deep Blast Program (DBP) Blast #3; (c) DBP Blast #7; (d) DBP Blast #17; (e) DBP Blast #20; (f) DBP Blast #28; (g) 30s particle velocity time history at TGP S8 and comparison of the body waves and phases for vertically separated TGPs S7 and S8 located within Borehole B-4 for the (h) Shallow Blast Program (SBP) Blast #3; (i) SBP Blast #8; (j) SBP Blast #12; (k) SBP Blast #23; and (l) SBP Blast #29.

due to its plasticity, permeability, and compressibility, which results in a higher characteristic frequency (Ishihara 1968). In contrast, the frequency of the near and far-field *SV*-waves are much lower than the *P*-wave and range from 7.7 Hz to 60 Hz in the Sand Array (Jana and Stuedlein 2021a) and 9 to 45 Hz in the Silt Array (Jana and Stuedlein 2022), are responsible for the predominant average frequencies measured (Fig. S1), and generally decreased from the higher to the lower ends of the ranges cited due to the softening of the deposits as the blast programs progressed. Due to their very high frequencies, the *P*-wave produces small particle displacements compared to the low frequency $SV$-waves [Figs. S2(c and g)] and pass in a drained state as proposed theoretically by Ishihara (1968). The $P$-wave induced $u_e$ is elastic due to the relative incompressibility of water compared to the soil skeleton (Stokoe and Santamarina 2000). In contrast, the low frequency near-field $SV$-wave generated by the unloading of the $P$-wave, and the far-field $SV$-wave, produced large displacements [Figs. S2(b and f)], the resulting shear strains, and residual excess pore pressure, $u_{e,r}$ [Figs. S2(d and h)], associated with gross sliding of soil particles (Martin et al. 1975; Dobry et al. 1982; Jana and Stuedlein 2021a, 2022). The influence of the $P$-wave on the dynamic soil response is therefore small.

## In Situ Cyclic Shear Stress and Determination of the Equivalent Number of Cycles

The preceding discussion demonstrated that the observed blast-induced ground motions may be treated as planar waves (Fig. 3) and that $P$-wave s could not produce residual excess pore pressure and may therefore be neglected. The blast-induced shear stresses can therefore be calculated using (Joyner and Chen 1975)

$$\tau = \rho \cdot v \cdot V_s(\gamma) \tag{2}$$

where $\tau$ = shear stress; $\rho$ = density; $v$ = particle velocity; and $V_s(\gamma)$ = shear strain-dependent shear wave velocity. A low-pass 70 Hz filter was applied to the particle velocities to remove the $P$-wave from the recorded waveforms. The strain-dependent cross-hole $V_s$ was calculated directly from arrival times using the vertical component of the waveform recorded in two horizontally separated TGPs as described by Jana and Stuedlein (2021a, 2022). The corresponding $CSR$ is then calculated by normalizing the shear stress time history with the corresponding $\sigma'_{v0}$, equal to 101 and 109 kPa, and 256 and 231 kPa, in Elements 1 and 2 of the Silt and Sand Arrays, respectively.

Fig. 4 presents the MATLAB algorithm adapted from Verma et al. (2019) to determine the $CSR$ time history and the corresponding equivalent number of stress cycles, $N_{eq}$, for each particle velocity time history. Figs. 5(a–c and g–i) present examples of the filtered particle velocity records recorded in the Sand and Silt Arrays during the Deep and Shallow Blast Programs, respectively. Occasional high-frequency components of motion riding on the backbone near-field $SV$-waves were removed as a result of the filtering process. The corresponding $CSR$ time histories are presented in Figs. 5(d–f and j–l) for the Sand and Silt Arrays, respectively. Following the calculation of each $CSR$ time history, the MATLAB script (Fig. 4) counts each positive and negative half cycle, $i$, in the time history and stores the absolute maximum $CSR_i$ of each half-cycle [e.g., Fig. 5(d)]. In the next step, the global maximum $CSR_i$ is stored in the variable $CSR_{max}$, equal to 0.13 for DBP Blast #30 [Fig. 5(e)]. Then for each half cycle, if the ratio of $CSR_i$ and $CSR_{max}$ is less than 0.10, the corresponding $CSR_i$ is removed and the half-cycle count, $i$ is updated (Idriss and Boulanger 2004). Fig. 5(e) shows that there are four half-cycles (circled) for which $CSR_i > 0.1CSR_{max}$. The equivalent number of stress cycles, $N_{eq}$ is then calculated for a given reference $CSR$, $CSR_{ref}$, and a known or assumed exponent $b$ (e.g., Fig. 2) describing the variation of $CSR$ with $N$ using (Idriss and Boulanger 2008)

$$N_{eq} = \frac{1}{2}\sum_{i=1}^{i}\left[\left(\frac{CSR_i}{CSR_{ref}}\right)^{\frac{1}{b}}\right] \tag{3}$$

For Deep Blast Program Blast #30 with $CSR_{max} = 0.13$ and $CSR_{ref} = 0.12$ and $b = 0.125$ [Fig. 2(a)], $N_{eq} = 1.81$. In the case

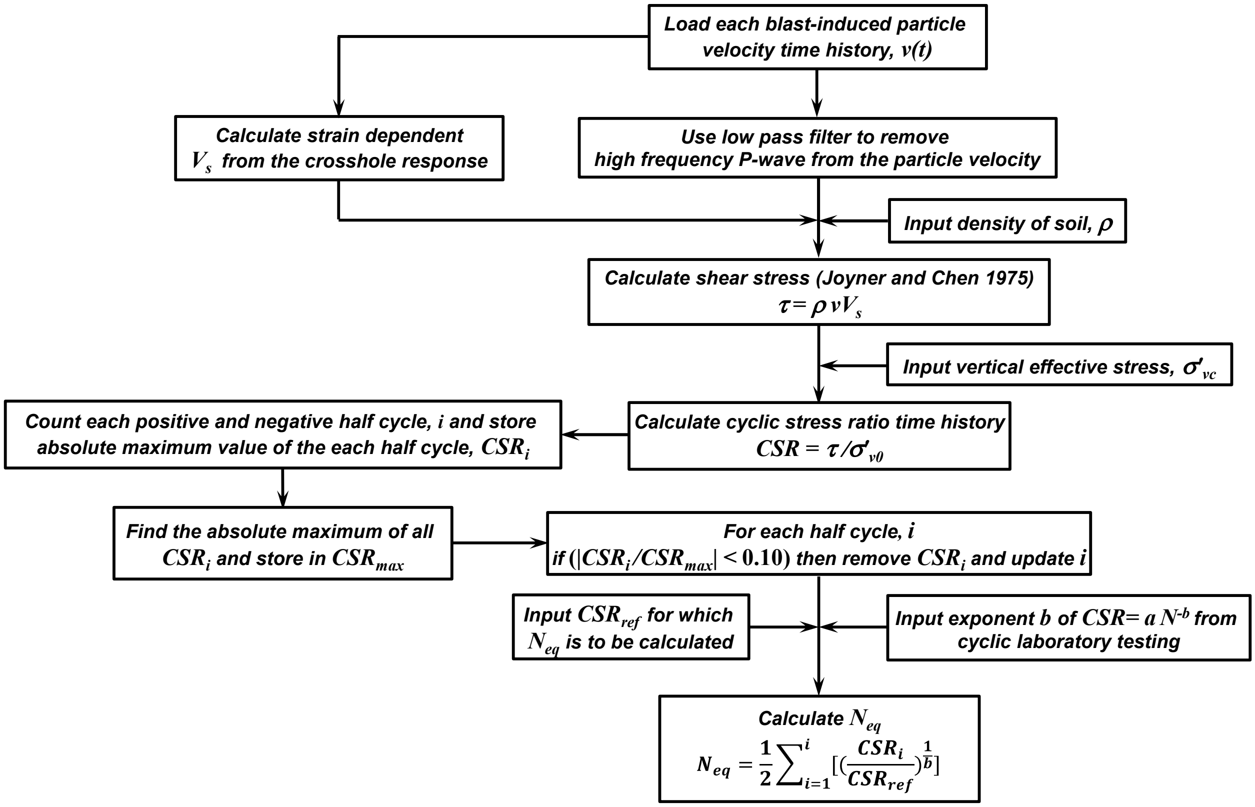

**Fig. 4.** Flowchart to determine equivalent number of stress cycles, $N_{eq}$ from blast-induced particle velocity time history. [Modified from Verma et al. (2019).]

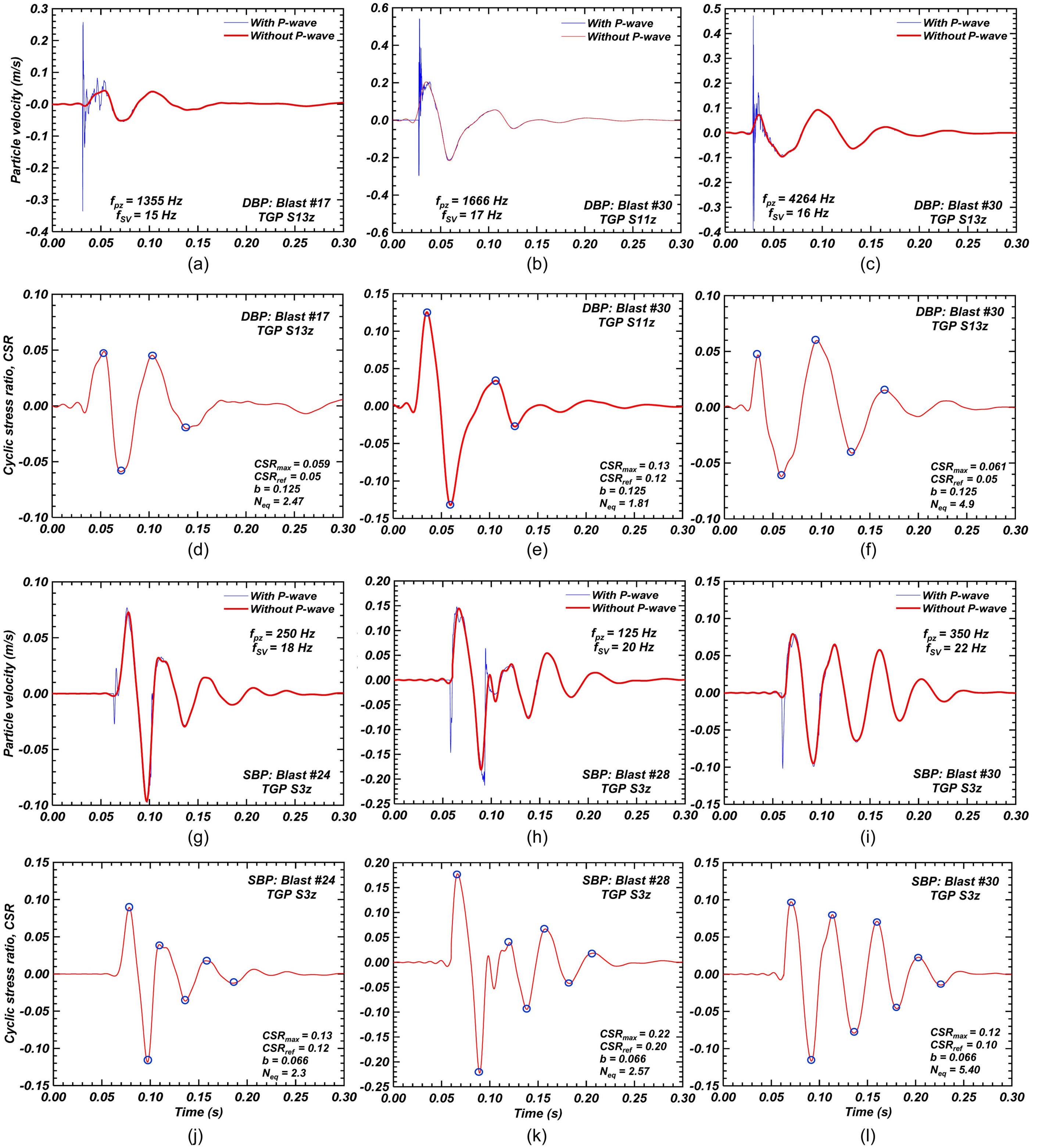

**Fig. 5.** Measured and filtered particle velocity time histories demonstrating removal of $P$-waves for the Sand and Silt Arrays: (a) Deep Blast Program (DBP) Blast #17 in TGP S13z; (b) DBP Blast #30 in TGP S11z; (c) DBP Blast #30 in TGP S13z; and cyclic stress ratio (CSR) time histories indicating $CSR_{max}$, $CSR_{ref}$, and $N_{eq}$ during (d) DBP Blast #17 in TGP S13z; (e) DBP Blast #30 in TGP S11z; and(f) DBP Blast #30 in TGP S13z; measured and filtered particle velocity time histories for (g) Shallow Blast Program (SBP) Blast #24 in TGP S3z; (h) SBP Blast #28 in TGP S3z; and (i) SBP Blast #30 in TGP S3z and CSR time histories for (j) SBP Blast #24 in TGP S3z; (k) SBP Blast #28 in TGP S3z; and (l) SBP Blast #30 in TGP S3z.

of SBP Blast #30 [Fig. 5(l)], the computed $CSR_{max} = 0.12$ and $N_{eq} = 5.40$ for $CSR_{ref} = 0.10$ and $b = 0.066$ [Fig. 2(b)].

Fig. 6 presents examples of full and individual, longitudinal and transverse $CSR$ time histories computed for the Sand and Silt Arrays during the Deep and Shallow Blast Programs, respectively. The strain-dependent $V_s$ determined from the vertical (transverse) component of the crosshole velocity was also used to determine the $CSR$ in the longitudinal components due to the lack of significant

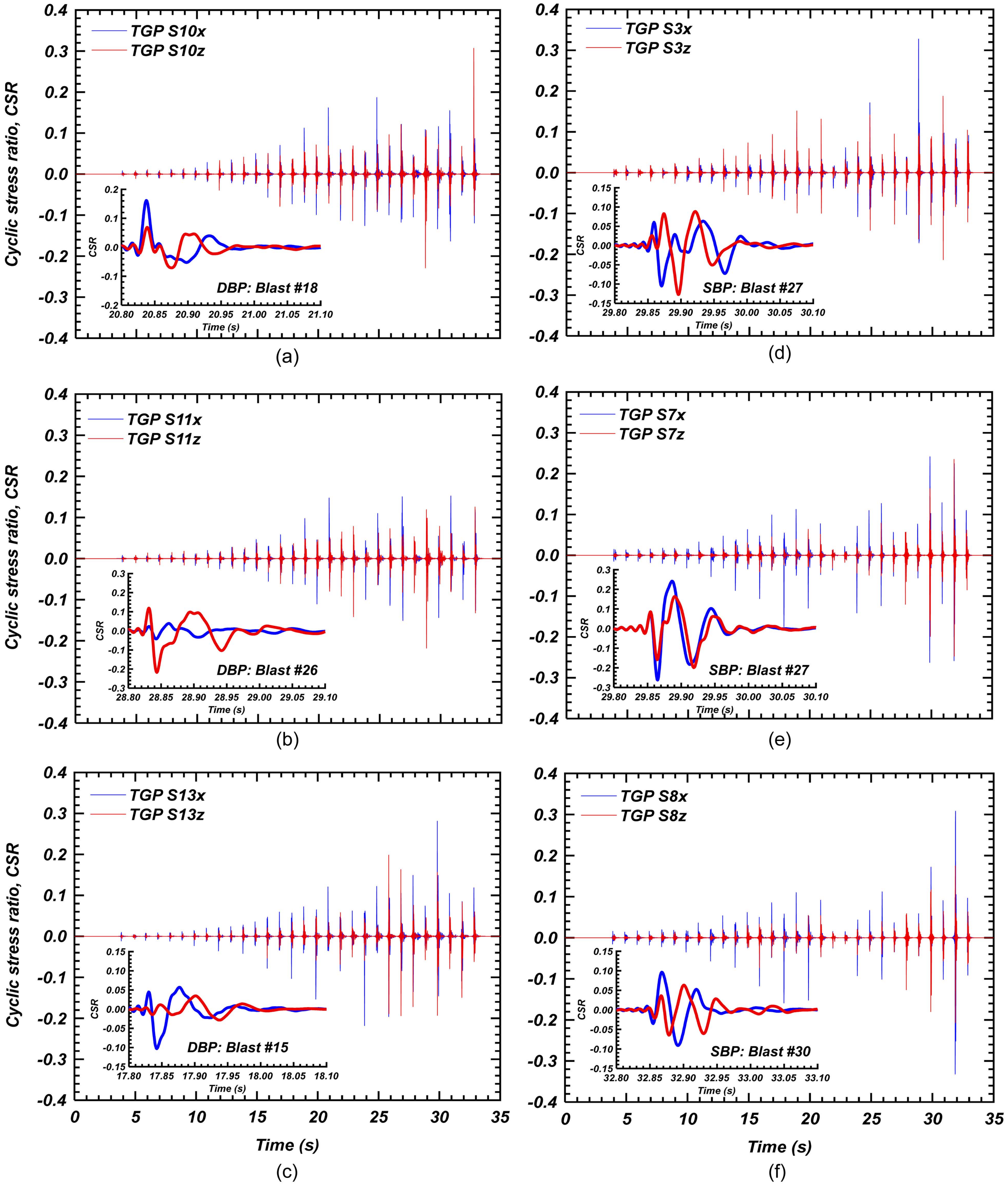

(a) (d)

(b) (e)

(c) (f)

**Fig. 6.** Variation of *CSR* time history in the Sand Array during the Deep Blast Program (DBP): (a) TGP S10; (b) TGP S11; (c) TGP S13, the variation of *CSR* time history in the Silt Array during the Shallow Blast Program (SBP); (d) TGP S3; (e) TGP S7; and (f) TGP S8.

anisotropy in $V_s$ measured in the sand and silt deposits (Donaldson 2019). In some instances [e.g., Figs. 6(a, c, and f)], the amplitude of the longitudinal *CSR* was largest, whereas in other detonations the amplitude of the transverse or vertical *CSR* was largest [e.g., Figs. 6(b and d)] or equal [Fig. 6(e)] to the longitudinal *CSR*. It is evident in Fig. 6 that blast-induced ground motions produce multidirectional shaking to provide an experimental basis for studying the effects thereof.

Figs. 7(a and c) present the variation of $CSR_{max}$ for each blast-induced waveform with scaled distance, $S_c = (R/W)^{1/3}$, defined as the ray path distance divided by the cubed root of the charge weight, in each TGP for the Sand and Silt Arrays and the Deep and Shallow Blast Programs, respectively. Figs. 7(b and d) present the variation of average *CSR*, $CSR_{avg}$, defined as the average *CSR* for all $N/2 > 0.1(CSR_{max})$ over the full waveform and for a minimum $CSR \geq 0.01$, and $N$ for each blast-induced waveform with $S_c$.

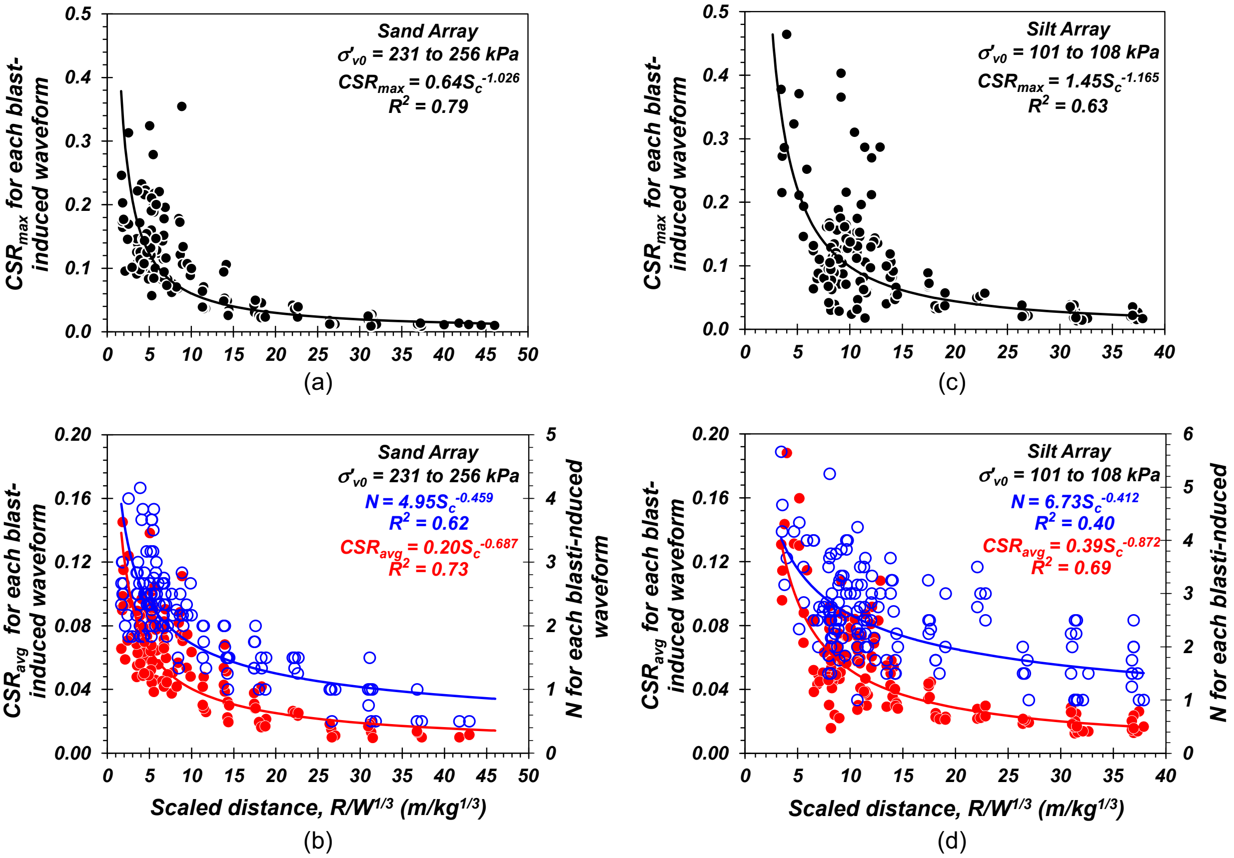

**Fig. 7.** Variation of cyclic stress ratios and number of cycles with scaled distance, including: (a) $CSR_{max}$; (b) $CSR_{avg}$ and $N_{eq}$ for the Sand Array during the Deep Blast Program; (c) $CSR_{max}$; and (d) $CSR_{avg}$ and $N_{eq}$ for the Silt Array during the Shallow Blast Program.

The scatter in the dataset of $CSR_{max}$ and $N$ with $S_c$ appears largest at smaller scaled distances, when the soil experienced significant and complex nonlinear-inelasticity and generation and dissipation of excess pore pressures (Jana and Stuedlein 2021a, 2022). Nonetheless, $CSR_{max}$, $CSR_{avg}$, and $N$ exhibit moderate to strong correlation, and increases with decreases in $S_c$. The maximum of $CSR_{max}$, $CSR_{avg}$, and $N$ calculated for every blast-induced waveform within the Sand Array is equal to 0.36, 0.15, and 4, respectively, whereas the maximum $CSR_{max}$, $CSR_{avg}$, and $N$ for every waveform within the Silt Array is equal 0.46, 0.19, and 9, respectively.

For the same $S_c$, $CSR_{max}$ was greater in the Silt Array than the Sand Array despite the smaller charges used, which is attributed to the smaller $\sigma'_{v0}$ in the Silt Array. The larger $r_{u,r}$ generated in the Sand Array ($r_{u,r} = 64\%$) compared to the Silt Array ($r_{u,r} = 13\%$) led to greater degradation in shear stiffness of the sand deposit (Jana and Stuedlein 2021a, 2022). The number of cycles inherent within a given single blast-induced waveform measured in the Silt Array [Fig. 7(d)] is larger than that in the Sand Array [Fig. 7(b)] at given $S_c$ as a result of the smaller exponent $b$ in the $CSR$-$N$ power law, as expected from the simplified method for liquefaction triggering analysis (Boulanger and Idriss 2015). Indeed, the total number of cycles with $CSR > 0.01$ in the Sand and Silt Arrays during the DBP and SBP equaled 49 and 86, respectively. The attenuation of $CSR_{max}$, $CSR_{avg}$, and $N$ with $S_c$ (Fig. 7) should prove useful for the design of future blast-liquefaction programs.

## Comparison of the In Situ Cyclic Resistance to Laboratory and Simplified Methods

### *Summary of Dynamic Responses of the Medium Dense Sand Deposit*

The shear strain time history deduced for the Sand Array during the 30 s Deep Blast Program presented by Jana and Stuedlein (2021a) demonstrated a direct link between the $\gamma_{DSS,max}$ and $r_{u,r}$ [see Figs. S3(a and b)]. The $\gamma_{DSS}$ imposed by the first two and three charges for Elements 1 and 2, respectively, resulted in zero residual excess pore pressure, $u_{e,r}$, and correspond to $CSR$s that are lower than 0.02. The threshold shear strain to initiate $u_{e,r}$ and $\gamma_{tp}$ of the natural sand deposit ranged from 0.008% to 0.01% for the intact, natural deposit corresponding reduction in normalized shear modulus, $G$ of approximately $0.70G_{max}$ (Jana and Stuedlein 2021a). As the charge weights and corresponding $CSR$s increased [inset of Fig. S3(a)], $r_{u,r}$ accumulated steadily with each additional charge. The Deep Blast Program produced $\gamma_{DSS,max}$ of 1.371% and 1.200% for Elements 1 and 2, respectively, and resulted in $r_{u,max}$ and $r_{u,r}$ of 64% and 53% in Element 1, and 72% and 57% in Element 2, respectively. The $CSR_{max}$ during the Deep Blast Program was approximately 0.36 [Fig. 7(a)], associated with a small charge located approximately 3 m from the center of the Sand Array. Global drainage initiated in the Sand Array following Blast #22 in Element 1 and Blast #27 in Element 2 under the established hydraulic gradient (Fig. 8), indicating that dynamic response in situ did not occur in a fully undrained state for the entirety of the experiment, unlike the response expected from constant-volume or undrained shearing

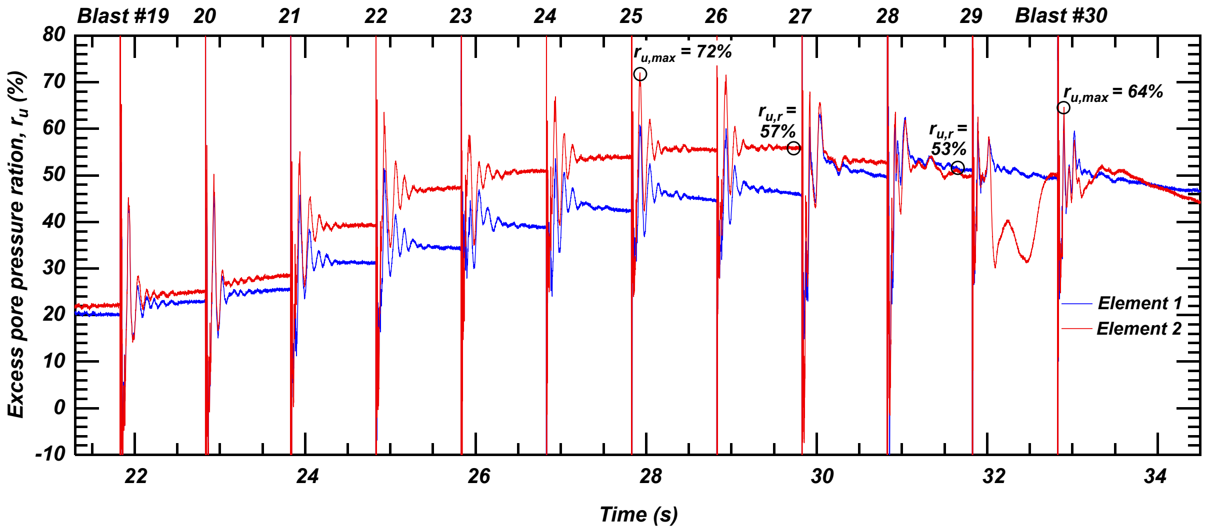

**Fig. 8.** In situ excess pore pressure response of the Sand Array during the Deep Blast Program in terms of the excess pore pressure ratio, $r_u$, indicating the initiation of drainage following Blast #22 in Element 1 and Blast #27 in Element 2.

performed on laboratory element test specimens. The partial drainage led to higher nonlinear shear modulus of the intact sand deposit and development of smaller $\gamma_{DSS}$ than would have been expected for a fully undrained response (Jana and Stuedlein 2021a), and its effect on cyclic resistance is addressed in the following section.

## Comparison of the In Situ Response to Cyclic DSS Specimens and Case History-Based Liquefaction Triggering Models

The $CRR$-$N_{eq}$ curves for Sand Array Elements 1 and 2 during the Deep Blast Program were developed by varying $CSR_{ref}$ to obtain the corresponding average $N_{eq}$ resulting from the average resultant $CSR$ vector (i.e., near-field dominant, longitudinal and far-field dominant, transverse particle velocities) provided by the four TGPs comprising the element as described in Fig. 4. This process was conducted for $b = 0.125$ and 0.22 to evaluate the role of the logarithmic slope of the assumed $CRR$-$N_{eq}$ power law for comparison to the cyclic DSS and case history-based cyclic resistances, as described below. Exponent $b = 0.22$ was selected to represent the average $q_{c1Ncs} = 98$ over the depths of the Sand Array based on the $q_{c1Ncs}$-$b$ relationship proposed by Boulanger and Idriss (2015) to provide an alternative to that derived from the reconstituted DSS specimens (i.e., $b = 0.125$), since cone penetration resistance reflects the large strain soil response corresponding to the in situ state. During the Deep Blast Program, the observed $r_{u,max}$ in the Sand Array was 72% and less than the typical 95% to 100% considered to represent initial triggering of liquefaction. Fig. 2(a) demonstrated that the difference between $CRR$ for the $\gamma_{SA} = 3\%$ and $r_{u,max} = 72\%$ cyclic failure criteria was negligible, suggesting that the comparison of the in situ $CRR$ with the laboratory-based $CRR$ at $r_{u,max} = 72\%$ is reasonable.

Fig. 9(a) presents the $CRR$-$N_{eq}$ curve for the two elements corresponding to the measured $r_{u,max}$ and $r_{u,r}$ of 64% and 53%, and 72% and 57%, in Elements 1 and 2, respectively, and for the entire Deep Blast Program. The in situ cyclic resistance derived from the $CRR$-$N_{eq}$ relationship is higher in Element 1 than Element 2, which is corroborated by the lower $u_e$ that developed in Element 1 [Figs. 8 and S3(b)]. The in situ $CRR$ at $N_{eq} = 15$ equals 0.22 and 0.21 in Elements 1 and 2, respectively, corresponding to a moment magnitude, $M_w = 7.5$ and exponent $b = 0.125$. Although the largest $\gamma_{DSS,max}$ (i.e., 1.371%) occurred in Element 1, inspection of Fig. S3(a) reveals that $\gamma_{DSS}$ and $r_u$ was lower in Element 1 than Element 2 until Blast #28, after which partial drainage inhibited further generation of residual $u_e$ despite the shear strain amplitude.

Fig. 9(a) also compares the in situ and laboratory test-based cyclic resistance for the Sand Array corresponding to exponent $b = 0.125$ determined from the uniaxial stress-controlled cyclic DSS tests [Fig. 2(a)]. The in situ cyclic resistance is clearly greater than that obtained from the reconstituted sand specimens sheared using the same $\sigma'_{v0}$, $D_r$, and $V_s$. For example, the in situ $CRR = 0.22$ and is ~50% larger than that of the reconstituted specimens ($CRR = 0.14$) for $N = 15$. The larger in situ cyclic resistance is attributed to the natural soil fabric developed over the age of the deposit, despite the multidirectional shaking imposed by the blast-induced ground motions. Note that the laboratory $CRR$ represents uniaxial cyclic loading and has not been reduced to account for the effects of multidirectional shaking, the reduction of which is generally assumed equal to 10% for sands (Idriss and Boulanger 2008). The difference between the in situ and laboratory $CRR$ derived in the present study agrees with that determined from frozen and cored, and unfrozen sampled sands with $D_r \approx 50\%$ reported by Yoshimi et al. (1984). Moreover, the partial drainage that occurred during the last stages of the Deep Blast Program may have also contributed to the larger in situ cyclic resistance as has been suggested by Wang et al. (2019), Adamidis et al. (2019), and Ni et al. (2021); this aspect is explored in detail below.

Case history- and in situ test-based simplified liquefaction triggering models set within the cyclic stress approach, including those using SPT (e.g., Boulanger and Idriss 2014; Cetin et al. 2018), CPT (e.g., Moss et al. 2006; Boulanger and Idriss 2014), and $V_s$ (e.g., Andrus and Stokoe 2000; Kayen et al. 2013), were used to compute the $CRR$ for $\sigma'_{v0} = 240$ kPa deduced for the Sand Array for the purposes of comparison. Initially, Boulanger and Idriss (2004) used $b = 0.34$ to represent clean sand based on the results of cyclic tests on frozen samples reported by Yoshimi et al. (1984). However, $b$ varies with $D_r$, soil fabric, and cementation, among other factors (Boulanger and Idriss 2015; Verma et al. 2019; Zamani and Montoya 2019). The revised CPT- and SPT-based liquefaction triggering models proposed by Boulanger and Idriss (2014, 2015) implemented an exponent $b$ which increases with increases in $D_r$, and $b = 0.22$ corresponds to the measured average

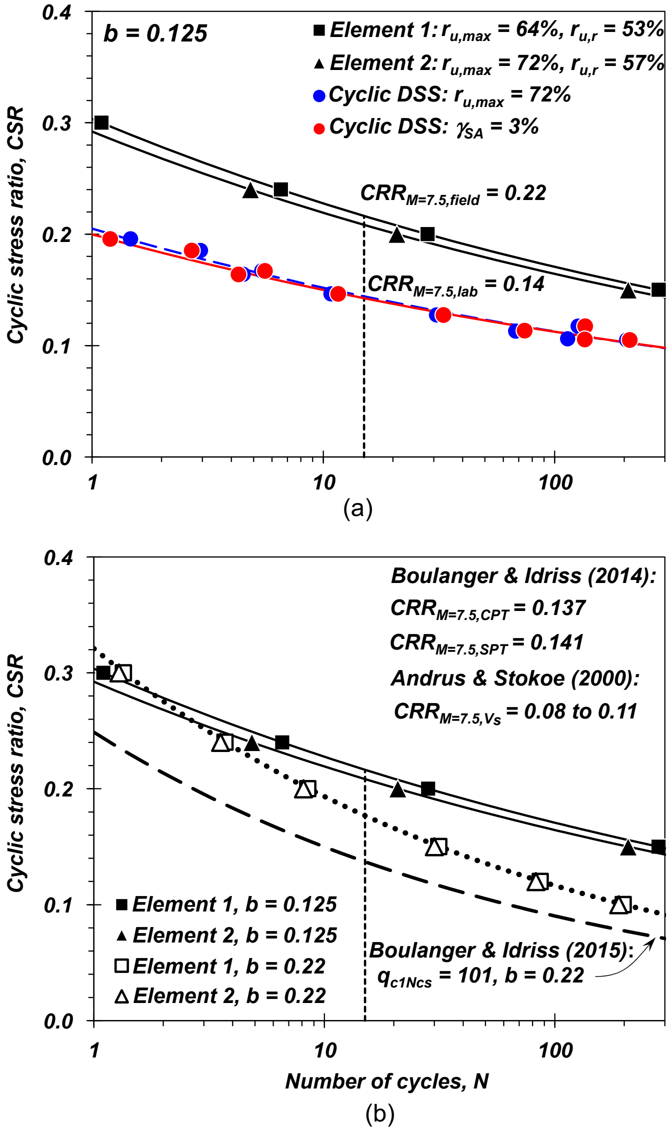

(a)

(b)

**Fig. 9.** In situ and laboratory test-based liquefaction triggering relationships derived for the Sand Array: (a) variation of *CSR* with *N* in Elements 1 and 2 and comparison to the laboratory-derived cyclic resistance of specimens reconstituted to the $D_r$, $V_s$, and $\sigma'_{vc}$ of the Sand Array; and (b) variation of *CSR* with *N* considering exponents $b = 0.125$ and 0.22.

$q_{c1Ncs} = 98$ for the Sand Array, larger than that determined for the reconstituted sand specimens (i.e., 0.125). Fig. 9(b) indicates the role of exponent $b$ on the in situ *CRR* derived for the Sand Array, and that for both exponents, the in situ cyclic resistance is greater than that suggested by Boulanger and Idriss (2015). Note that the cyclic resistance derived from the in situ dynamic testing corresponds to $r_{u,max} = 64\%$ to 72% and $\gamma_{DSS,max} = 1.2\%$ to 1.371%, both of which are lower than that assumed in liquefaction triggering criteria of simplified methods (generally $r_{u,max} = 100\%$ or $\gamma_{SA} = 3\%$). The observed difference between the in situ cyclic resistance and that of the Boulanger and Idriss (2015) simplified method is attributed in part to the relationship between penetration resistance and laboratory cyclic resistance selected in the development of the method. In the derivation of *CRR*, exponent $b$ in the Boulanger and Idriss (2015) simplified method depends on $D_r$ only, however $b$ can vary with other parameters of soil such as *FC*, *PI*, particle angularity, failure strain criterion, and other factors, and the need for site-specific adjustments to penetration test-based *CRR* has been hypothesized (Boulanger and Idriss 2015). The controlled blasting test method described herein serves as a direct method for the evaluation of in situ cyclic resistance and provide a basis for site-specific adjustments to penetration and $V_s$ test-based *CRR*.

Calculations of $CRR_{Mw=7.5}$ made using CPT- (Moss et al. 2006; Boulanger and Idriss 2014), SPT- (Boulanger and Idriss 2012; Cetin et al. 2018), and $V_s$- based models (Andrus and Stokoe 2000; Kayen et al. 2013) returned cyclic resistance ratios that range from 0.08 to 0.15 considering probability of liquefaction, $P_L$, of 15%, typically associated with the deterministic *CRR* (Table 1). Laboratory test-based $CRR_{M=7.5}$ derived using bender element-based $V_s$ and DSS tests are equal to 0.12 and 0.14, respectively (Table 1). In contrast, the in situ $CRR_{N=15}$ ranged from 0.18 to 0.22 for $b = 0.22$ and 0.125, respectively, and the SPT-, CPT-, $V_s$-, and DSS test-based *CRR*s ranges from 36% to 83% of the in situ *CRR* (Table 1).

Whereas the loading and resistance is known (or deterministic) during the Deep Blast Program within the potential error associated with measurements of particle velocity, assumptions regarding blast-induced ground motions (i.e., 2D versus 3D; influence of the *P*-wave), and reliability of the selected exponents $b$, liquefaction triggering models include uncertainty in the loading and resistance. Thus, the comparison of *CRR* for $P_L = 15\%$ (i.e., commonly representing the deterministic *CRR*) may not be strictly appropriate. Table 1 thus presents the SPT-, CPT-, and $V_s$-based $CRR_{Mw=7.5}$ for $P_L = 50\%$ and 85% where possible, representing the median *CRR* and median *CRR* plus one standard deviation. The lowest estimate of the in situ *CRR* (i.e., 0.18) appears to be associated with $P_L = 85\%$ for the Boulanger and Idriss (2014) SPT- and CPT-based liquefaction triggering models, and $P_L = 50\%$ for the Moss et al. (2006) CPT-based model. In contrast, the probabilistic models by Cetin et al. (2018; SPT) and Kayen et al. (2013; $V_s$) provide lower *CRR* than that in situ for $P_L$ up to 85% (Table 1).

The range in $CRR_{Mw=7.5}$ derived from the penetration, shear wave velocity, and laboratory test techniques is large, indicating significant differences between the calibration of the selected simplified methods, and the potential for large differences from the $CRR_{Mw=7.5}$ deduced from the in situ experiments described herein. This comparison also provides indirect evidence for the effect of partial drainage on the overburden stress correction factor, $K_\sigma$, through comparison of the SPT- and CPT-based triggering models. The ratio of in situ and $K_\sigma$-corrected, penetration test-based, deterministic (i.e., $P_L = 15\%$) $CRR_{Mw=7.5}$ ranges from 1.29 ($b = 0.22$) to 1.57 ($b = 0.125$). This finding appears to confirm centrifuge test-based observations of the effect of high overburden stresses and partial drainage on cyclic resistance reported by Ni et al. (2021). Partial drainage was observed in Elements 1 and 2 after the passage of the ground motions associated with Blasts #22 and #27, respectively, associated with the latter stages of the Deep Blast Program (Fig. 8). Since the effect of partial drainage is inherently included in the assessments of *CRR* described above, the undrained cyclic resistance of the Sand Array was estimated by considering *only* those *CSR* time histories up to Blasts #22 and #27 in Elements 1 and 2, respectively, as drainage initiated *after* passage of the corresponding *S*-waves. Fig. 10 presents the comparison of *CRR* versus *N* of the Sand Array elements considering partially drained (associated with the full *CSR* time history; Fig. 9) and undrained conditions (associated with the truncated *CSR* time histories). The undrained $CRR_{Mw=7.5}$ of Elements 1 and 2 is 0.20 and 0.14, and 0.20 and 0.16, for $b = 0.125$ and 0.22, respectively. Thus, the partially drained sand deposit exhibited 6% to 27% larger

**Table 1.** Comparison of cyclic resistances computed for the Sand Array ($\sigma'_{v0} = 240$ kPa) using various methods

| Test method | Reference | Resistance term | Overburden stress correction, $K_\sigma$ | $CRR_{M=7.5}$ | Percent of in situ, $CRR_{M=7.5}$ (%) |
|---|---|---|---|---|---|
| SPT | Boulanger and Idriss (2012, 2014) | $N_{1,60cs} = 15$ bpf | 0.90 | | |
| | | $P_L = 15\%$ | | 0.14 | 64 to 78 |
| | | $P_L = 50\%$ | | 0.16 | 73 to 89 |
| | | $P_L = 85\%$ | | 0.18 | 82 to 100 |
| | Cetin et al. (2018) | $N_{1,60cs} = 15$ bpf | N/A | | |
| | | $P_L = 15\%$ | | 0.08 | 36 to 44 |
| | | $P_L = 50\%$ | | 0.10 | 45 to 56 |
| | | $P_L = 85\%$ | | 0.13 | 59 to 72 |
| CPT | Boulanger and Idriss (2014, 2015) | $q_{c1Ncs} = 98$ | 0.88 | | |
| | | $P_L = 15\%$ | | 0.12 | 55 to 67 |
| | | $P_L = 50\%$ | | 0.14 | 64 to 78 |
| | | $P_L = 85\%$ | | 0.18 | 82 to 100 |
| | Moss et al. (2006) | $q_{c,1} = 8.52$ MPa | N/A | | |
| | | $P_L = 15\%$ | | 0.15 | 68 to 83 |
| | | $P_L = 50\%$ | | 0.19 | 86 to 106 |
| | | $P_L = 85\%$ | | 0.24 | 109 to 133 |
| Downhole, $V_s$ | Andrus and Stokoe (2000) | $V_{s1} = 151$ to 170 m/s | N/A | 0.08 to 0.11 | 36 to 56 |
| | Kayen et al. (2013) | $V_{s1} = 151$ to 170 m/s | N/A | | |
| | | $P_L = 15\%$ | | 0.08 to 0.10 | 36 to 56 |
| | | $P_L = 50\%$ | | 0.10 to 0.13 | 45 to 72 |
| | | $P_L = 85\%$ | | 0.13 to 0.17 | 59 to 94 |
| Controlled blasting | — | $b = 0.125$ | N/A | 0.22 | N/A |
| | | $b = 0.22$ | | 0.18 | N/A |
| Laboratory | — | — | — | $0.14^a$ | 64 to 78 |
| | $V_s$ (Andrus and Stokoe 2000) | $V_{s1} = 175$ m/s | N/A | $0.12^b$ | 55 to 67 |

Note: $P_L$ = probability of liquefaction; and N/A = not applicable.
[a]Cyclic DSS test results on reconstituted specimens.
[b]Bender Element tests on reconstituted cyclic DSS test specimens.

$CRR_{Mw=7.5}$ than that estimated for undrained conditions, depending on the assumed exponent $b$. Although use of the truncated $CSR$ time histories necessarily will result in lower $CRR$s, due in part to the loss of high-shear stress loading cycles, these findings confirm observations that partial drainage can increase cyclic resistance under high overburden stress conditions, the increase of which was noted equal to about 20% based on centrifuge tests (Ni et al. 2020). In contrast, the effects of partial drainage on the $CRR$ implied by liquefaction triggering models is essentially unknown. Nonetheless, the estimated undrained $CRR$ computed using the truncated $CSR$ time histories reduces the differences with the liquefaction model-based $CRR$s summarized in Table 1.

### Summary of Dynamic Responses of the Silt Deposit

Similar to the Sand Array, the cyclic response within the Silt Array can be described in terms of $\gamma_{DSS}$, $r_{u,r}$, and $CSR$ over the 30 s Shallow Blast Program. Shear strain accumulated from nonlinear elastic regime to the nonlinear inelastic regime, achieving $\gamma_{DSS,max}$ and corresponding $r_{u,r}$ of 0.35% and 12.6%, and 0.22% and 8.2%, for Elements 1 and 2, respectively [Figs. S3(c and d), Jana and Stuedlein 2022]. The initial $r_{u,r}$ in Element 2 was greater than that of Element 1 due to the larger initial shear strain; however, temporary drainage during the latter half of the Shallow Blast Program, prior to the reversal of drainage when the last two charges were detonated, resulted in a corresponding stiffer response in Element 2, inhibiting significant further $\gamma_{DSS}$ and $r_{u,r}$ relative to Element 1. Accumulation of $r_{u,r}$ in the Silt Array correlates well with $\gamma_{DSS}$ (Jana and Stuedlein 2022), whereas no distinct trend between the $CSR$ and $r_u$ time histories can be observed [compare Figs. 6(d–f) and S3(d)].

### Comparison of In Situ and Laboratory-Based Cyclic Resistances

In contrast to cohesionless deposits, the laboratory test-based cyclic resistance developed from intact specimens of plastic soils is anticipated to provide a more appropriate basis for comparison to the in situ cyclic resistance. Accordingly, $CRR$-$N_{eq}$ curves were developed for Elements 1 and 2 of the Silt Array by varying $CSR_{ref}$ to obtain the corresponding average $N_{eq}$ for the limited $r_{u,max}$ and $r_{u,r}$ that developed during the Shallow Blast Program and compared alongside the cyclic resistance of the intact silt specimens. Fig. 11(a) presents the in situ $CRR$-$N_{eq}$ curve determined using exponent $b = 0.066$ ($\gamma_{SA} = 3\%$) to those corresponding to $r_{u,max}$ and $r_{u,r}$ of 29% and 13% in Element 1, and 31% and 8% in Element 2, respectively. The $CRR$ for $N = 30$ cycles ($M_w = 7.5$; Idriss and Boulanger 2008), $CRR_{N=30} = 0.33$ and 0.29, for Elements 1 and 2, respectively (Table 2). The cyclic stress ratio of Element 1 is slightly larger than that of Element 2, due in part to the higher $\gamma_{DSS}$ and $r_{u,r}$ in Element 1 [Figs. S3(c and d); note that Element 1 exhibited lower $r_{u,max}$]. The comparison of the in situ cyclic resistance developed using $b = 0.066$ may not be appropriate given that $\gamma_{DSS,max} = 0.35\%$ and smaller, whereas the laboratory $CRR$-$N$ curve corresponds to the $\gamma_{SA} = 3\%$ cyclic failure criterion.

Inspection of Fig. 2(b) shows that the curvature of the laboratory $CRR$-$N$ curve is significantly greater ($b = 0.17$) for limited excess pore pressure generation (such as that observed in situ) than the large strain $\gamma_{SA} = 3\%$ cyclic failure criterion ($b = 0.066$), and that the scatter in the cyclic resistance is greater for the $r_{u,r}$ criterion than the $r_{u,max}$ criterion. Thus, it is of interest to compare the in situ $CRR$-$N_{eq}$ curves developed using laboratory-derived,

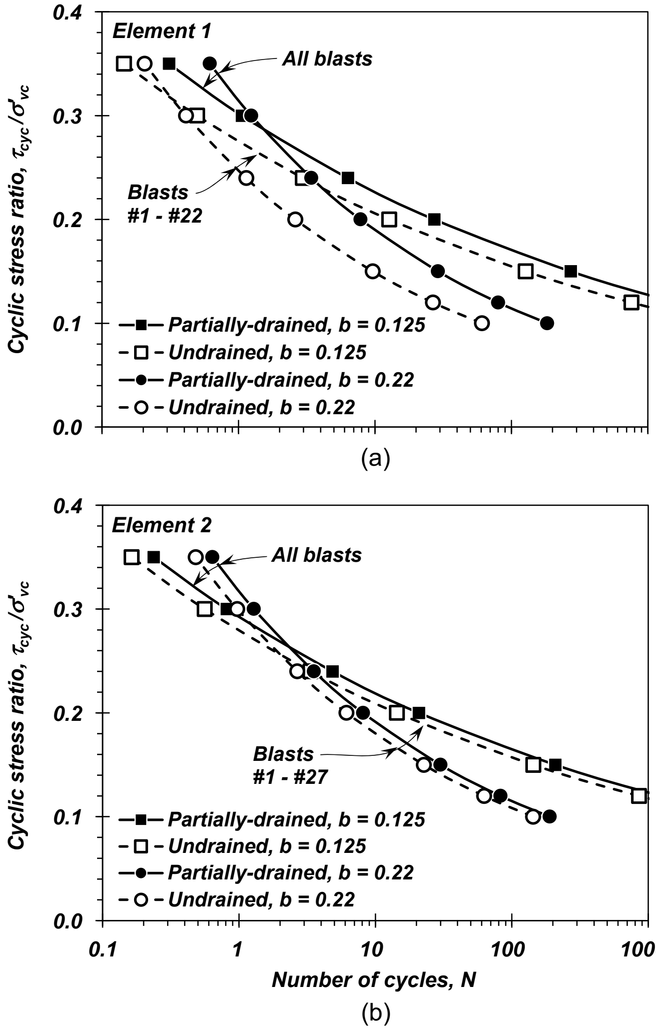

**Fig. 10.** Comparison of the in situ cyclic resistance of the Sand Array considering partially drained and undrained conditions: (a) Element 1; and (b) Element 2.

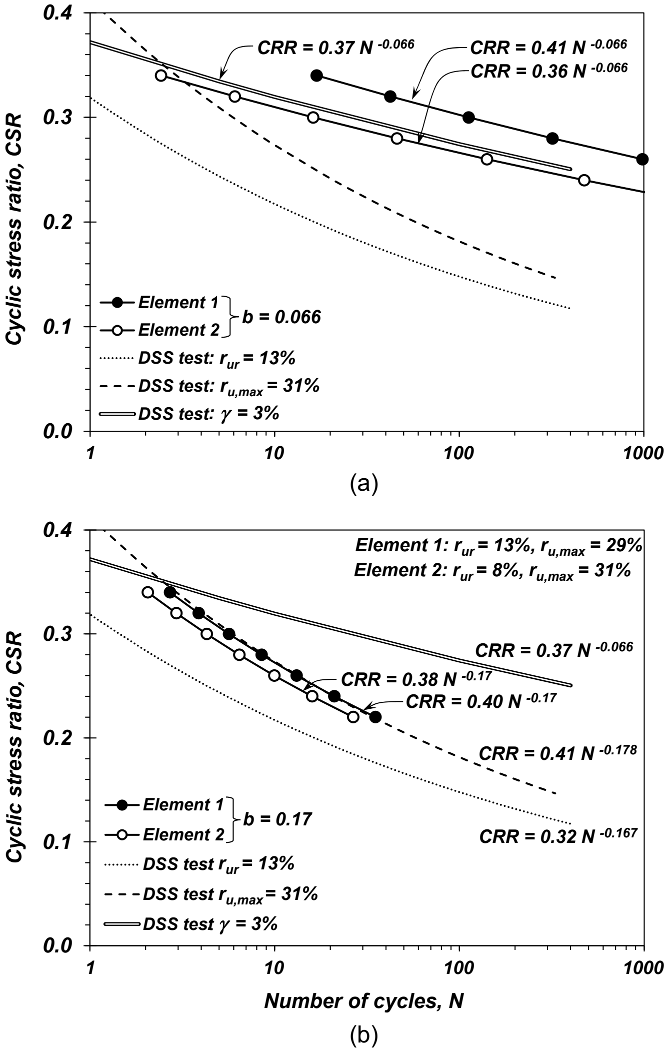

**Fig. 11.** Comparison of in situ and laboratory test-based cyclic resistance derived for Elements 1 and 2 in the Silt Array: (a) assuming $b = 0.066$ ($\gamma_{SA}$–3%) for the in situ cyclic resistance; and (b) assuming $b = 0.17$ (assuming $r_{u,max}$ and $r_{u,r}$-based exponents) for the in situ cyclic resistance.

$r_u$-consistent cyclic failure criteria. Fig. 11(b) presents such in situ $CRR\text{-}N_{eq}$ curves for $b = 0.17$ and limited $r_{u,max}$ and $r_{u,r}$ [Fig. 2(b)]. The $CRR_{N=30}$ for the two elements ranges narrowly from 0.215 to 0.225, corresponding to ~75% of that determined using $b = 0.066$, and is best matched by the $r_{u,max}$ laboratory *CRR-N* curve. Note that the in situ $CRR\text{-}N_{eq}$ curves inherently includes the effects of multidirectional shaking, and yields a *CRR* that is 0% to 7% smaller (for $N_{eq}$ ranging from 1 to 100) than that based on $r_{u,max}$ and uniaxial laboratory shaking. Previous researchers have suggested that the reduction in *CRR* for multidirectional shaking of plastic soil deposits should be approximately 4% (e.g., Idriss and Boulanger 2008), which appears consistent with the in situ cyclic resistance determined in this study and within the potential error associated with measurements of particle velocity and assumptions regarding blast-induced ground motions

The in situ cyclic resistance strongly depends on the assumed exponent $b$ used to construct the $CRR\text{-}N_{eq}$ curves. Comparison of the $r_{u,max}$-based laboratory and in situ (and $r_{u,max}$-based $b = 0.17$) *CRR-N* curves demonstrates that use of a consistent stress-based cyclic failure criterion, in the current case $r_{u,max}$, results in the best agreement in cyclic resistance [Fig. 11(b)]. Additional in situ dynamic testing to larger excess pore pressure magnitudes would allow confirmation and guidance on the selection of an appropriate exponent for use in conversion of transient waveforms to uniform shear stress loading cycles.

## Concluding Remarks

This study presents the in situ cyclic resistance of liquefiable, medium dense sand, and cyclic softening-susceptible silt deposits using controlled blasting as a source of seismic energy. Characterization of the blast-induced ground motions justified two assumptions necessary to calculate the cyclic shear stress from the particle velocity records. First, the frequency of the blast-induced *P*-waves is too large to pass in an undrained state, and accordingly were filtered from the full particle velocity waveforms prior computing cyclic shear stresses. Second, the body waves passing through the observation window (i.e., the scale of measurement) were generally observed to share amplitudes and phases; accordingly, the seismic waveforms were assumed to be planar, and facilitated simplified computation of the strain-dependent cyclic shear stresses. Calculation of the shear stresses from the particle velocity records allowed

**Table 2.** Comparison of cyclic resistance for the Silt Array during the Shallow Blast Program to various laboratory-based measurements

| Test method | Cyclic failure criterion | Exponent, $b$ | $CRR_{N=15}$ | $CRR_{N=30}$ |
|---|---|---|---|---|
| Cyclic DSS on intact specimens | $\gamma_{SA} = 3\%$ | 0.066 | 0.31 | 0.30 |
| | $r_{u,max} = 31\%$ | 0.178 | 0.25 | 0.22 |
| | $r_{u,r} = 13\%$ | 0.167 | 0.18 | 0.20 |
| In situ, Element 1 | $r_{u,max} = 29\%$, $r_{u,r} = 13\%$ | 0.066 | 0.34 | 0.33 |
| | $r_{u,max} = 29\%$, $r_{u,r} = 13\%$ | 0.170 | 0.25 | 0.22 |
| In situ, Element 2 | $r_{u,max} = 31\%$, $r_{u,r} = 8\%$ | 0.066 | 0.30 | 0.29 |
| | $r_{u,max} = 31\%$, $r_{u,r} = 8\%$ | 0.170 | 0.24 | 0.21 |

the determination of the equivalent number of stress cycles, $N_{eq}$, through consideration of known and assumed exponents of the laboratory test-based power laws describing the variation of cyclic resistance ratio, *CRR*, with uniform loading cycles. This in turn facilitated development of the relationship between the in situ *CRR* with $N_{eq}$, and the variation of both with scaled distance for the instrumented Sand and Silt Arrays, respectively, within the error of the field measurements and selected *CRR-N* exponents. Based on the observations stemming from this study, the following may be concluded:

1. The maximum value among all $CSR_{max}$, $CSR_{avg}$, and $N$ calculated for blast-induced waveforms in the Sand Array was 0.36, 0.15, and 4, respectively, whereas the maximum $CSR_{max}$, $CSR_{avg}$, and $N$ calculated the waveforms in the Silt Array was 0.46, 0.19, and 9, respectively.
2. The $CSR_{max}$, $CSR_{avg}$, and $N$ decreases with scaled distance; the corresponding trends presented herein could be useful for the design of controlled blasting programs to obtain various constitutive soil properties or characterize large strain behavior.
3. The *CRR*-$N_{eq}$ relationship determined for the Sand Array demonstrated that the in situ cyclic resistance was greater than that obtained from cyclic DSS tests conducted on sand specimens reconstituted to the in situ vertical effective stress, $\sigma'_{v0}$, relative density, $D_r$, and small strain shear wave velocity, $V_s$. Laboratory test-based $CRR_{M=7.5}$ derived from bender element test-based $V_s$ and cyclic DSS tests was equal to 0.12 and 0.14, respectively, significantly smaller than $CRR_{M=7.5} = 0.22$ deduced for in situ conditions.
4. The difference between the in situ and laboratory test-based *CRR* for the Sand Array is attributed to the differences in the soil fabric between the natural in situ sand and laboratory specimens. Partial drainage during the latter stages of the controlled blasting experiment appears to have contributed to the greater cyclic resistance of the sand deposit relative to the imposed constant-volume boundary conditions associated with the DSS test specimens.
5. The $CRR_{Mw=7.5}$ derived using deterministic case history-based liquefaction triggering models implementing in situ penetration tests (SPT, CPT) and downhole $V_s$ measurements and commonly associated with a probability of liquefaction, $P_L$, of ~15%, was 36 to 83% smaller than the in situ $CRR_{Mw=7.5}$, suggesting that (1) there are large differences in the calibration of these triggering relationships stemming from different modeling decisions and using different liquefaction case history databases; (2) the actual in situ *CRR* appears considerably larger than that implied by some of liquefaction triggering models considered; and (3) centrifuge test-based observations of the effect of partial drainage and high overburden stress on $K_\sigma$ reported by Ni et al. (2021) appear confirmed.
6. The lower range of the in situ *CRR* (i.e., 0.18) considering the effects of partial drainage appears to be associated with $P_L = 50$ to 85% for several probabilistic liquefaction models, whereas others provide lower *CRR* than that in situ for $P_L$ up to 85%. Truncation of the blast-induced *CSR* time histories to estimate the fully undrained, in situ *CRR* reduced the differences between the estimated in situ *CRR* and that computed using these liquefaction triggering models. The undrained, in situ *CRR* was 6% to 27% smaller than that computed using the full *CSR* time histories associated with partial drainage towards the latter stages of the experiment.
7. The in situ *CRR* determined for the Sand and Silt Arrays depends strongly on the assumed logarithmic slope of the *CRR-N* curve, *b*. Evaluation of the cyclic resistance of the Silt Array, where the shear strains and excess pore pressures were small (relative to the Sand Array) indicated that the use of maximum excess pore pressure–compatible *CRR-N* curves appears necessary for conversion of irregular seismic waveforms to uniform loading cycles.
8. The use of excess pore pressure–consistent cyclic resistance criteria to deduce the *CRR* for the Silt Array suggests that reductions to stress-based cyclic resistance for multidirectional shaking of plastic deposits ranges from 0% to 7% for $N_{eq}$ ranging from 1 to 100.

## Data Availability Statement

Some or all data, models, or code that support the findings of this study are available from the corresponding author upon reasonable request.

## Acknowledgments

The authors gratefully acknowledge the sponsorship of this work by Cascadia Lifelines Program (CLiP) and its members, with special thanks to member agency Port of Portland. The authors were supported by the National Science Foundation (Grant CMMI 1663654) during the course of these experiments. Any opinions, findings, and conclusions expressed are those of the authors and do not necessarily reflect the views of the above-mentioned sponsors.

## Supplemental Materials

Figs. S1–S3 are available online in the ASCE Library (www.ascelibrary.org).

## References

Abdoun, T., M. A. Gonzalez, S. Thevanayagam, R. Dobry, A. Elgamal, M. Zeghal, and U. El Shamy. 2013. "Centrifuge and large-scale modeling of seismic pore pressures in sands: Cyclic strain interpretation." *J. Geotech. Geoenviron. Eng.* 139 (8): 1215–1234. https://doi.org/10.1061/(ASCE)GT.1943-5606.0000821.

Adamidis, O., U. Sinan, and I. Anastasopoulos. 2019. "Effects of partial drainage on the response of Hostun sand: An experimental investigation at element level." In Vol. 4 of *Earthquake geotechnical engineering for protection and development of environment and constructions*, 993–1000. Boca Raton, FL: CRC Press.

Andrus, R. D., and K. H. Stokoe II. 2000. "Liquefaction resistance of soils from shear-wave velocity." *J. Geotech. Geoenviron. Eng.* 126 (11): 1015–1025. https://doi.org/10.1061/(ASCE)1090-0241(2000)126:11(1015).

Ashford, S. A., R. W. Boulanger, J. L. Donahue, and J. P. Stewart. 2011. *Geotechnical quick report on the Kanto plain region during the March 11, 2011, Off Pacific coast of Tohoku earthquake, Japan*. Rep. No. GEER-025a. Berkeley, CA: Geotechnical Extreme Events Reconnaissance.

Beyzaei, C. Z., J. D. Bray, M. Cubrinovski, M. Riemer, and M. E. Stringer. 2018. "Laboratory-based characterization of shallow silty soils in southwest Christchurch." *Soil Dyn. Earthquake Eng.* 110 (Jul): 93–109. https://doi.org/10.1016/j.soildyn.2018.01.046.

Boulanger, R. W., and I. M. Idriss. 2004. *Evaluating the potential for liquefaction or cyclic failure of silts and clays*. Rep. No. UCD/CGM-04/01. Davis, CA: Univ. of California.

Boulanger, R. W., and I. M. Idriss. 2007. "Evaluation of cyclic softening in silts and clays." *J. Geotech. Geoenviron. Eng.* 133 (6): 641–652. https://doi.org/10.1061/(ASCE)1090-0241(2007)133:6(641).

Boulanger, R. W., and I. M. Idriss. 2012. "Probabilistic standard penetration test–based liquefaction–triggering procedure." *J. Geotech. Geoenviron. Eng.* 138 (10): 1185–1195. https://doi.org/10.1061/(ASCE)GT.1943-5606.0000700.

Boulanger, R. W., and I. M. Idriss. 2014. *CPT and SPT based liquefaction triggering procedures*. Rep. No. UCD/CGM-14/01. Davis, CA: Center for Geotechnical Modelling.

Boulanger, R. W., and I. M. Idriss. 2015. "Magnitude scaling factors in liquefaction triggering procedures." *Soil Dyn. Earthquake Eng.* 79 (Dec): 296–303. https://doi.org/10.1016/j.soildyn.2015.01.004.

Boulanger, R. W., and R. B. Seed. 1995. "Liquefaction of sand under bidirectional monotonic and cyclic loading." *J. Geotech. Eng.* 121 (12): 870–878. https://doi.org/10.1061/(ASCE)0733-9410(1995)121:12(870).

Cetin, K. O., R. B. Seed, R. E. Kayen, R. E. S. Moss, H. T. Bilge, M. Ilgac, and K. Chowdhury. 2018. "SPT-based probabilistic and deterministic assessment of seismic soil liquefaction triggering hazard." *Soil Dyn. Earthquake Eng.* 115 (Dec): 698–709. https://doi.org/10.1016/j.soildyn.2018.09.012.

Chang, N. Y., S. T. Yeh, and L. P. Kaufman. 1982. "Liquefaction potential of clean and silty sands." In Vol. 2 of *Proc., 3rd Int. Earthquake Microzonation Conf.*, 1017–1032. Washington, DC: National Science Foundation.

Chang, W. J., E. M. Rathje, K. H. Stokoe, and K. Hazirbaba. 2007. "In situ pore pressure generation behavior of liquefiable sand." *J. Geotech. Geoenviron. Eng.* 133 (8): 921–931. https://doi.org/10.1061/(ASCE)1090-0241(2007)133:8(921).

Cox, B. R., K. H. Stokoe, and E. M. Rathje. 2009. "An in-situ test method for evaluating the coupled pore pressure generation and nonlinear shear modulus behavior of liquefiable soils." *Geotech. Test. J.* 32 (1): 11–21.

Cubrinovski, M., et al. 2010. "Geotechnical reconnaissance of the 2010 Darfield (Canterbury) earthquake." *Bull. N. Z. Soc. Earthquake Eng.* 43 (4): 243–320. https://doi.org/10.5459/bnzsee.43.4.243-320.

Cubrinovski, M., A. Rhodes, N. Ntritsos, and S. Van Ballegooy. 2019. "System response of liquefiable deposits." *Soil Dyn. Earthquake Eng.* 124 (Sep): 212–229. https://doi.org/10.1016/j.soildyn.2018.05.013.

Dahl, K., R. W. Boulanger, and J. T. DeJong. 2018. "Trends in experimental data of intermediate soils for evaluating dynamic strength." In *Proc., 11th US National Conf. on Earthquake Engineering*. Los Angeles: Earthquake Engineering Research Institute.

Dahl, K. R., J. T. DeJong, R. W. Boulanger, R. Pyke, and D. Wahl. 2014. "Characterization of an alluvial silt and clay deposit for monotonic, cyclic, and post-cyclic behavior." *Can. Geotech. J.* 51 (4): 432–440. https://doi.org/10.1139/cgj-2013-0057.

Dobry, R., and T. Abdoun. 2015a. "3rd Ishihara Lecture: An investigation into why liquefaction charts work: A necessary step toward integrating the states of art and practice." *Soil Dyn. Earthquake Eng.* 68 (Jan): 40–56. https://doi.org/10.1016/j.soildyn.2014.09.011.

Dobry, R., and T. Abdoun. 2015b. "Cyclic shear strain needed for liquefaction triggering and assessment of overburden pressure factor $k_\sigma$." *J. Geotech. Geoenviron. Eng.* 141 (11): 04015047. https://doi.org/10.1061/(ASCE)GT.1943-5606.0001342.

Dobry, R., R. S. Ladd, F. Y. Yokel, R. M. Chung, and D. Powell. 1982. *Prediction of pore water pressure buildup and liquefaction of sands during earthquakes by the cyclic strain method*. Rep. No. 138. Gaithersburg, MD: National Bureau of Standards.

Donaldson, A. M. 2019. "Characterization of the small-strain stiffness of soils at an in-situ liquefaction test site." M.S. thesis, School of Civil and Construction Engineering, Oregon State Univ.

El-Sekelly, W., T. Abdoun, and R. Dobry. 2016. "Liquefaction resistance of a silty sand deposit subjected to preshaking followed by extensive liquefaction." *J. Geotech. Geoenviron. Eng.* 142 (4): 04015101. https://doi.org/10.1061/(ASCE)GT.1943-5606.0001444.

El-Sekelly, W., R. Dobry, T. Abdoun, and J. H. Steidl. 2017. "Two case histories demonstrating the effect of past earthquakes on liquefaction resistance of silty sand." *J. Geotech. Geoenviron. Eng.* 143 (6): 04017009. https://doi.org/10.1061/(ASCE)GT.1943-5606.0001654.

Esposito, M. P., III, and R. D. Andrus. 2017. "Peak shear strength and dilatancy of a pleistocene age sand." *J. Geotech. Geoenviron. Eng.* 143 (1): 04016079. https://doi.org/10.1061/(ASCE)GT.1943-5606.0001582.

Evarts, R., J. O'Connor, and R. Wells. 2009. "The Portland Basin: A (big) river runs through it." *GSA Today* 19 (9): 4–10. https://doi.org/10.1130/GSATG58A.1.

Finn, W. D. L., P. L. Bransby, and D. J. Pickering. 1970. "Effect of strain history on liquefaction of sand." *J. Soil Mech. Found. Div.* 96 (6): 1917–1934. https://doi.org/10.1061/JSFEAQ.0001478.

Franke, K. W., R. D. Koehler, C. Z. Beyzaei, A. Cabas, I. Pierce, A. Stuedlein, and Z. Yang. 2019. *Geotechnical engineering reconnaissance of the 30 November 2018 Mw 7.0 Anchorage, Alaska earthquake*. GEER Rep. No. GEER-059. Geotechnical Extreme Events Association. https://doi.org/10.18118/G6P07F.

Idriss, I. M., and R. W. Boulanger. 2004. "Semi-empirical procedures for evaluating liquefaction potential during earthquakes." In Vol. 11 of *Proc., 11th Int. Conf. on Earthquake Geotechnical Engineering*, edited by D. Doolin, et al., 32–56. Davis, CA: Stallion Press.

Idriss, I. M., and R. W. Boulanger. 2008. *Soil liquefaction during earthquakes*. Monograph MNO-12. Oakland, CA: Earthquake Engineering Research Institute.

Ishihara, K. 1968. "Propagation of compressional waves in a saturated soil." In *Proc., Int. Symp. Wave Propagation and Dynamic Properties of Earth Materials*, 195–206. Albuquerque, NM: Univ. of New Mexico Press.

Ishihara, K., K. Harada, W. F. Lee, C. C. Chan, and A. M. M. Safiullah. 2016. "Post-liquefaction settlement analyses based on the volume change characteristics of undisturbed and reconstituted samples." *Soils Found.* 56 (3): 533–546. https://doi.org/10.1016/j.sandf.2016.04.019.

Ishihara, K., and M. Yoshimine. 1992. "Evaluation of settlements in sand deposits following liquefaction during earthquakes." *Soils Found.* 32 (1): 173–188. https://doi.org/10.3208/sandf1972.32.173.

Jana, A. 2021. "Use of controlled blasting to quantify the dynamic, *in-situ*, nonlinear inelastic response of soils." Ph.D. dissertation, School of Civil and Construction Engineering, Oregon State Univ.

Jana, A., A. Dadashiserej, B. Zhang, A. W. Stuedlein, T. M. Evans, K. H. Stokoe II, and B. R. Cox. 2022. "Multi-directional vibroseis shaking and controlled blasting to determine the dynamic in-situ response of a low plasticity silt deposit." *J. Geotech. Geoenviron. Eng.* 149 (3): 04023006. https://doi.org/10.1061/(ASCE)GT.1943-5606.0002924.

Jana, A., A. M. Donaldson, A. W. Stuedlein, and T. M. Evans. 2021. "Deep, in-situ nonlinear dynamic testing of soil with controlled blasting: Instrumentation, calibration, and example application to a plastic silt deposit." *Geotech. Test. J.* 44 (5): 1301–1326. https://doi.org/10.1520/GTJ20190426.

Jana, A., and A. W. Stuedlein. 2021a. "Dynamic in-situ response of a deep, medium dense sand deposit." *J. Geotech. Geoenviron. Eng.* 147 (6): 04021039. https://doi.org/10.1061/(ASCE)GT.1943-5606.0002523.

Jana, A., and A. W. Stuedlein. 2021b. "Monotonic, cyclic and post-cyclic response of an alluvial plastic silt deposit." *J. Geotech. Geoenviron. Eng.* 147 (3): 04020174. https://doi.org/10.1061/(ASCE)GT.1943-5606.0002462.

Jana, A., and A. W. Stuedlein. 2022. "Dynamic, in situ, nonlinear-inelastic response and post-cyclic strength of a plastic silt deposit." *Can. Geotech. J.* 59 (1): 111–128. https://doi.org/10.1139/cgj-2020-0652.

Joyner, W. B., and A. T. Chen. 1975. "Calculation of nonlinear ground response in earthquakes." *Bull. Seismol. Soc. Am.* 65 (5): 1315–1336. https://doi.org/10.1785/BSSA0650051315.

Kayen, R., R. Moss, E. Thompson, R. Seed, K. Cetin, A. Kiureghian, Y. Tanaka, and K. Tokimatsu. 2013. "Shear-wave velocity–based probabilistic and deterministic assessment of seismic soil liquefaction potential." *J. Geotech. Geoenviron. Eng.* 139 (3): 407–419. https://doi.org/10.1061/(ASCE)GT.1943-5606.0000743.

Koester, J. P. 1994. "The influence of fines type and content on cyclic strength." In *Ground failures under seismic conditions*, 17–33. New York: ASCE.

Ladd, R. S. 1977. "Specimen preparation and cyclic stability of sands." *J. Geotech. Eng. Div.* 103 (6): 535–547. https://doi.org/10.1061/AJGEB6.0000435.

Ladd, R. S. 1978. "Preparing test specimens using under compaction." *Geotech. Test. J.* 1 (1): 16–23. https://doi.org/10.1520/GTJ10364J.

Lee, W. F., K. Ishihara, and C. C. Chen. 2012. "Liquefaction of silty sandpreliminary studies from recent Taiwan, New Zealand and Japan earthquakes." In *Proc., Int. Symp. on Engineering Lessons Learned from the 2011 Great East Japan Earthquake*, 747–758. Tokyo: Japan Association Earthquake Engineering.

Martin, G. R., W. D. L. Finn, and H. B. Seed. 1975. "Fundamentals of liquefaction under cyclic loading." *J. Geotech. Eng. Div.* 101 (5): 423–438. https://doi.org/10.1061/AJGEB6.0000164.

Moss, R. E. S., R. B. Seed, R. E. Kayen, J. P. Stewart, A. Der Kiureghian, and K. O. Cetin. 2006. "CPT-based probabilistic and deterministic assessment of in situ seismic soil liquefaction potential." *J. Geotech. Geoenviron. Eng.* 132 (8): 1032–1051. https://doi.org/10.1061/(ASCE)1090-0241(2006)132:8(1032).

Mulilis, J. P., C. K. Chan, and H. B. Seed. 1975. *The effects of method of sample preparation on the cyclic stress-strain behavior of sands*. EERC Rep. No. 75-18. Berkeley, CA: Univ. of California.

Ni, M., T. Abdoun, R. Dobry, and W. El-Sekelly. 2021. "Effect of field drainage on seismic pore pressure buildup and $K_\sigma$ under high overburden pressure." *J. Geotech. Geoenviron. Eng.* 147 (9): 04021088. https://doi.org/10.1061/(ASCE)GT.1943-5606.0002536.

Ni, M., T. Abdoun, R. Dobry, K. Zehtab, A. Marr, and W. El-Sekelly. 2020. "Pore pressure and K $\sigma$ evaluation at high overburden pressure under field drainage conditions. I: Centrifuge experiments." *J. Geotech. Geoenviron. Eng.* 146 (9): 04020088. https://doi.org/10.1061/(ASCE)GT.1943-5606.0002303.

Price, A., J. DeJong, and R. Boulanger. 2017. "Cyclic loading response of silt with multiple loading events." *J. Geotech. Geoenviron. Eng.* 143 (10): 04017080. https://doi.org/10.1061/(ASCE)GT.1943-5606.0001759.

Rathje, E., R. Phillips, W. J. Chang, and K. H. Stokoe. 2001. "Evaluating nonlinear response in situ." In *Proc., 4th Int. Conf. on Recent Advances in Geotechnical Earthquake Engineering and Soil Dynamics*. San Diego: Missouri S&T Library and Learning Resources.

Roberts, J. N., K. H. Stokoe, S. Hwang, B. R. Cox, Y. Wang, F. M. Menq, and S. van Ballegooy. 2016. "Field measurements of the variability in shear strain and pore pressure generation in Christchurch soils." In *Proc., 5th Int. Conf. on Geotechnical and Geophysical Site Characterization*. Sydney, NSW, Australia: Australian Geomechanics Society.

Robertson, P. 2009. "Interpretation of cone penetration tests—A unified approach." *Can. Geotech. J.* 46 (11): 1337–1355. https://doi.org/10.1139/T09-065.

Sahadewa, A., D. Zekkos, R. D. Woods, and K. H. Stokoe. 2015. "Field testing method for evaluating the small-strain shear modulus and shear modulus nonlinearity of solid waste." *Geotech. Test. J.* 38 (4): 20140016. https://doi.org/10.1520/GTJ20140016.

Sanin, M. V., and D. Wijewickreme. 2006. "Cyclic shear response of channel-fill Fraser River Delta silt." *Soil Dyn. Earthquake Eng.* 26 (9): 854–869. https://doi.org/10.1016/j.soildyn.2005.12.006.

Seed, H. B. 1979. "Soil liquefaction and cyclic mobility evaluation for level ground during earthquakes." *J. Geotech. Eng. Div.* 105 (2): 201–255. https://doi.org/10.1061/AJGEB6.0000768.

Seed, H. B., and K. L. Lee. 1965. *Studies of liquefaction of sands under cyclic loading conditions*. Rep. No. TE-65-65. Berkeley, CA: Univ. of California.

Seed, H. B., K. Tokimatsu, L. F. Harder, and R. M. Chung. 1985. "Influence of SPT procedures in soil liquefaction resistance evaluations." *J. Geotech. Eng.* 111 (12): 1425–1445. https://doi.org/10.1061/(ASCE)0733-9410(1985)111:12(1425).

Singh, S. 1994. "Liquefaction characteristics of silts." In *Ground Failures under Seismic Conditions*. Geotechnical Special Publication 44, 105–116. Reston, VA: ASCE.

Stokoe, K. H., II, and J. C. Santamarina. 2000. "Seismic-wave based testing in geotechnical engineering." In Vol. 1 of *Proc., Int. Conf. on Geotechnical and Geological Engineering*, 1490–1536. Brunswick, OH: Association of Environmental and Engineering Geologists.

Tasiopoulou, P., K. Ziotopoulou, F. Humire, A. Giannakou, J. Chacko, and T. Travasarou. 2020. "Development and implementation of semiempirical framework for modeling postliquefaction shear deformation accumulation in sands." *J. Geotech. Geoenviron. Eng.* 146 (1): 04019120. https://doi.org/10.1061/(ASCE)GT.1943-5606.0002179.

Troncoso, J. H., and R. Verdugo. 1985. "Silt content and dynamic behavior of tailings sands." In *Proc., 11th Int. Conf. on Soil Mechanics and Foundation Engineering*, 1311–1314. Rotterdam, Netherlands: A.A. Balkema.

Upadhyaya, S., R. A. Green, B. W. Maurer, A. Rodriguez-Marek, and S. van Ballegooy. 2022. "Limitations of surface liquefaction manifestation severity index models used in conjunction with simplified stress-based triggering models." *J. Geotech. Geoenviron. Eng.* 148 (3): 04021194. https://doi.org/10.1061/(ASCE)GT.1943-5606.0002725.

Verma, P., A. Seidalinova, and D. Wijewickreme. 2019. "Equivalent number of uniform cycles versus earthquake magnitude relationships for fine-grained soils." *Can. Geotech. J.* 56 (11): 1596–1608. https://doi.org/10.1139/cgj-2018-0331.

Wang, B., C. Yao, Z. Liu, H. Fan, and H. Xiao. 2019. "Development of an energy-based EPWP generation model under different drainage conditions." *IOP Conf. Ser.: Earth Environ. Sci.* 304 (2): 022053. https://doi.org/10.1088/1755-1315/304/2/022053.

Wijewickreme, D., A. Soysa, and P. Verma. 2019. "Response of natural fine-grained soils for seismic design practice: A collection of research findings from British Columbia, Canada." *Soil Dyn. Earthquake Eng.* 124 (Sep): 280–296. https://doi.org/10.1016/j.soildyn.2018.04.053.

Xiao, P., H. Liu, Y. Xiao, A. W. Stuedlein, and T. M. Evans. 2018. "Liquefaction resistance of bio-cemented calcareous sand." *Soil Dyn. Earthquake Eng.* 107 (Apr): 9–19. https://doi.org/10.1016/j.soildyn.2018.01.008.

Yoshimi, Y., K. Tokimatsu, and Y. Hosaka. 1989. "Evaluation of liquefaction resistance of clean sands based on high-quality undisturbed samples." *Soils Found.* 29 (1): 93–104. https://doi.org/10.3208/sandf1972.29.93.

Yoshimi, Y., K. Tokimatsu, and O. Kaneko. 1984. "Undrained cyclic shear strength of a dense Niigata sand." *Soils Found.* 24 (4): 131–145. https://doi.org/10.3208/sandf1972.24.4_131.

Youd, T. L., and I. M. Idriss. 2001. "Liquefaction resistance of soils: Summary report from the 1996 NCEER and the 1998 NCEER/NSF workshops on the evaluation of liquefaction resistance of soils." *J. Geotech. Geoenviron. Eng.* 127 (4): 297–313. https://doi.org/10.1061/(ASCE)1090-0241(2001)127:4(297).

Zamani, A., and B. M. Montoya. 2019. "Undrained cyclic response of silty sands improved by microbial induced calcium carbonate precipitation." *Soil Dyn. Earthquake Eng.* 120 (May): 436–448. https://doi.org/10.1016/j.soildyn.2019.01.010.

Zeghal, M., and A. W. Elgamal. 1994. "Analysis of site liquefaction using earthquake records." *J. Geotech. Eng.* 120 (6): 996–1017. https://doi.org/10.1061/(ASCE)0733-9410(1994)120:6(996).

Zeghal, M., A. W. Elgamal, H. T. Tang, and J. C. Stepp. 1995. "Lotung downhole array. II: Evaluation of soil nonlinear properties." *J. Geotech. Eng.* 121 (4): 363–378. https://doi.org/10.1061/(ASCE)0733-9410(1995)121:4(363).

# SUPPLEMENTAL MATERIALS

ASCE *Journal of Geotechnical and Geoenvironmental Engineering*

# On the In Situ Cyclic Resistance of Natural Sand and Silt Deposits

Armin W. Stuedlein, Amalesh Jana, Ali Dadashiserej,
and Xiao Yang

**DOI:** 10.1061/JGGEFK.GTENG-10784

www.ascelibrary.org

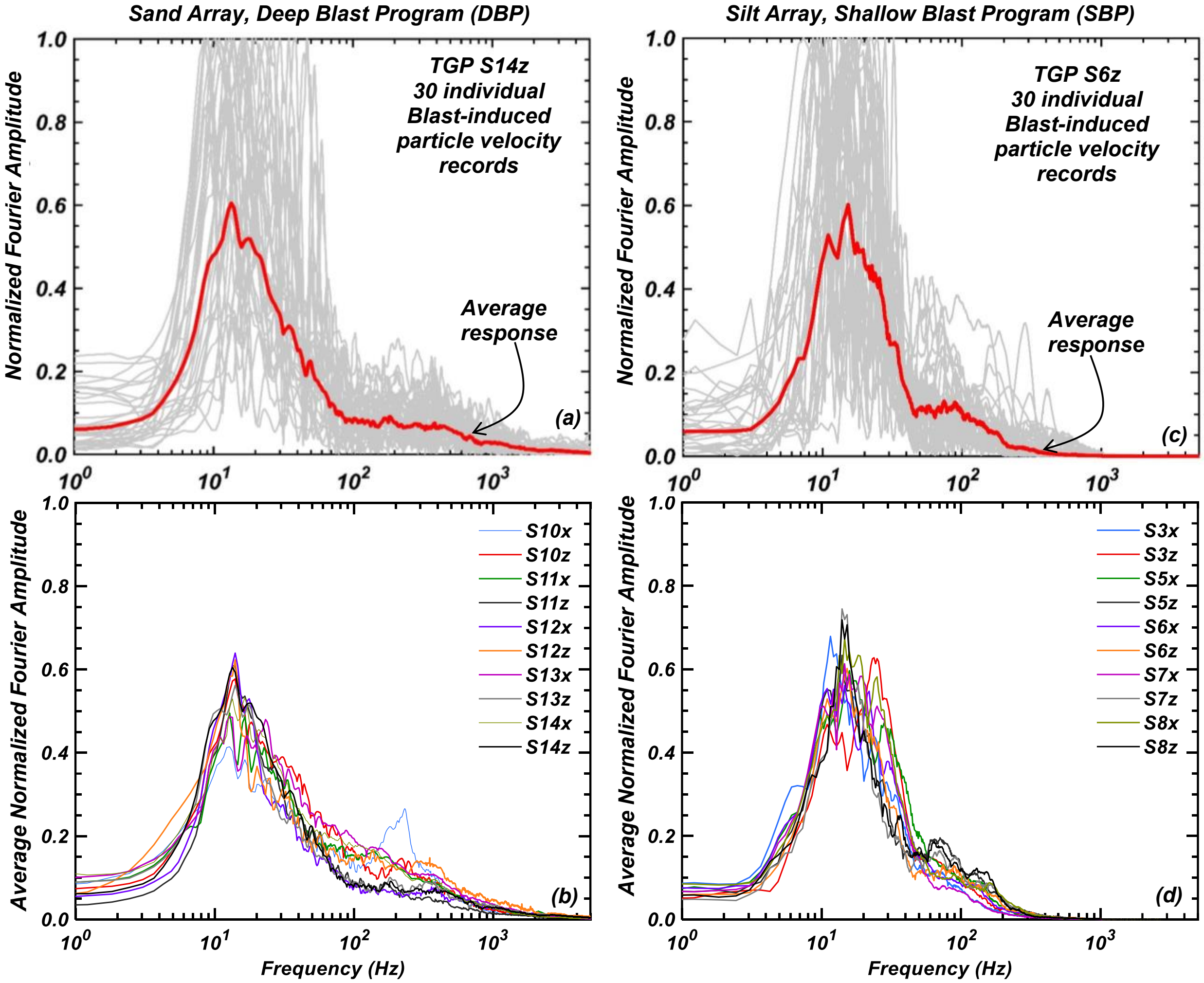

Sand Array, Deep Blast Program (DBP)

Silt Array, Shallow Blast Program (SBP)

**Fig. S1. Frequency content of the blast-induced ground motions in the Sand Array during the DBP, including: (a) normalized Fourier amplitude spectra for the 30 particle velocity records for TGP S14z and their average; (b) average normalized Fourier amplitude spectra for each TGP; and frequency content of ground motions in the Silt Array during the SBP; (c) normalized Fourier amplitude spectra for the particle velocity records of TGP S6z and their average; and (d) average normalized Fourier amplitude spectra for each TGP.**

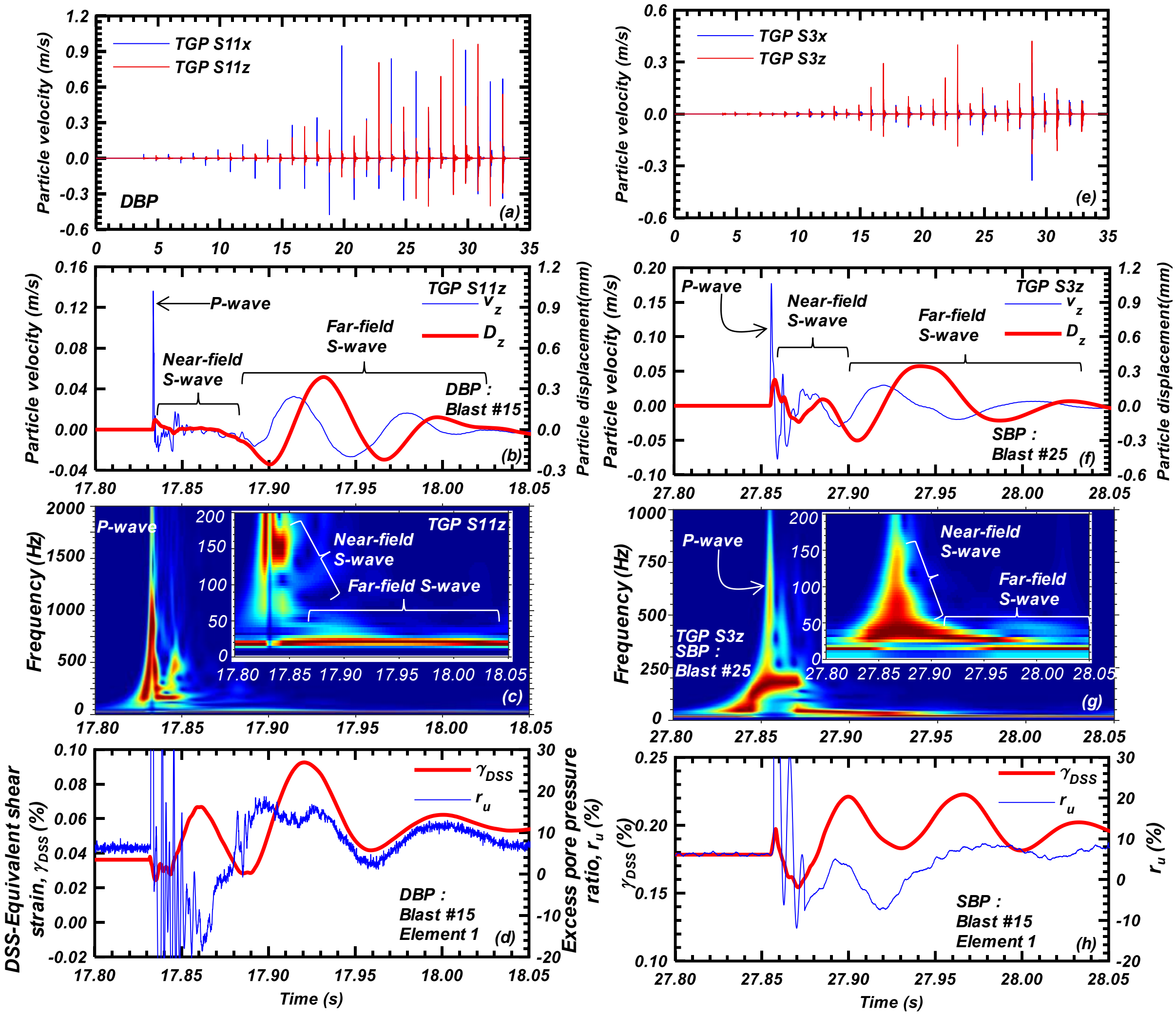

**Fig. S2.** Components of blast-induced motions and their effects, including (a) 30 s particle velocity time history of TGP S11 (Sand Array); and (b) particle velocity and corresponding particle displacement, (c) Stockwell spectrum of the of the vertical component of TGP S11, and (d) variation of shear strain and excess pore pressure response for DBP Blast # 15; and (e) 30 s particle velocity time history of TGP S3 (Silt Array); and (f) particle velocity and corresponding particle displacement, (g) Stockwell spectrum of the of vertical component of TGP S3, and (h) variation of shear strain and excess pore pressure response for SBP Blast # 25.

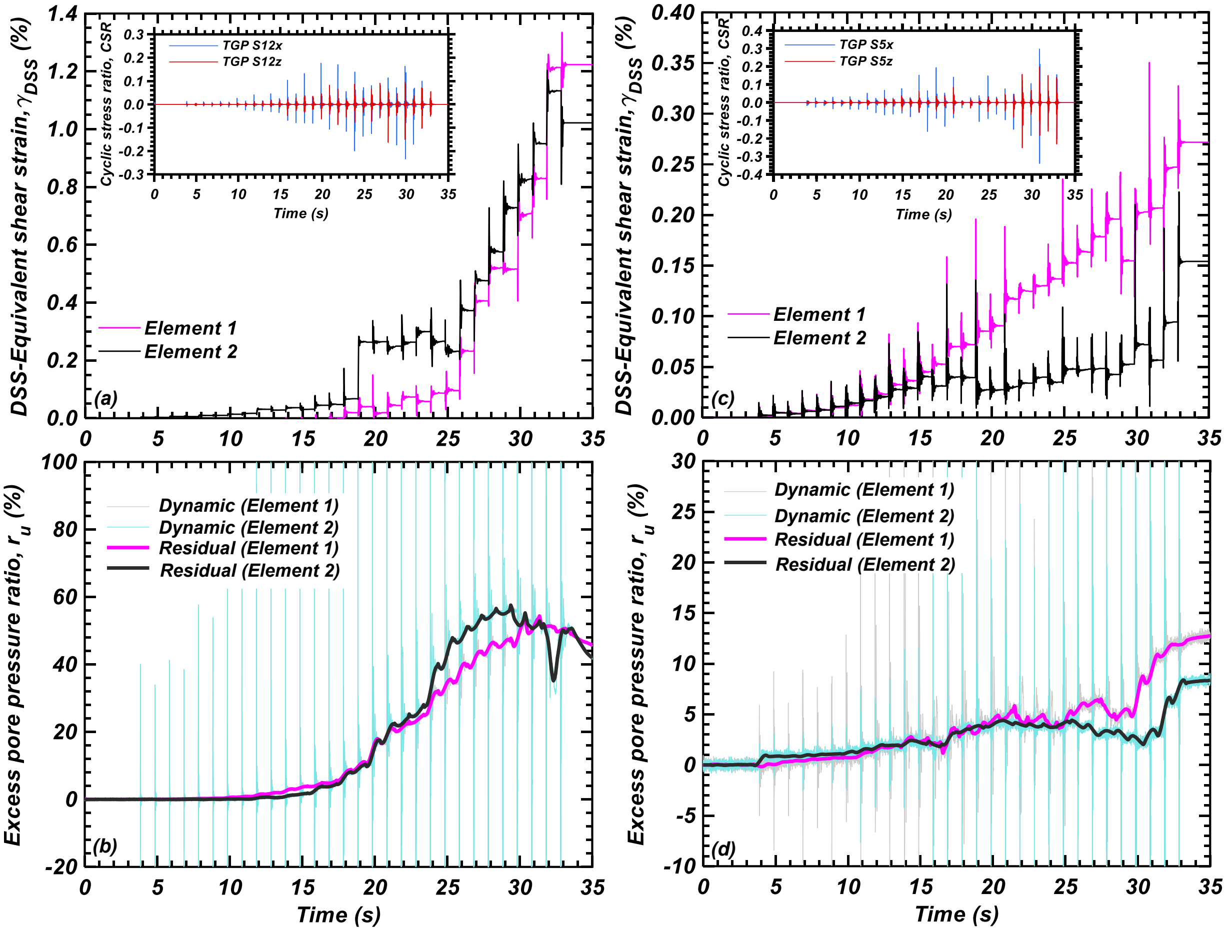

**Fig. S3. In-situ dynamic response of the Sand Array during the 30 s DBP (a) variation of DSS-equivalent shear strain, $\gamma_{DSS}$ (inset showing CSR time history in TGP S12), (b) generation of Dynamic and residual excess pore pressure ratio, $r_u$ in two elements of the Sand Array; dynamic response of the Silt Array during the 30 s SBP (c) variation $\gamma_{DSS}$ (inset showing CSR time history in TGP S5), (d) generation of $r_u$ in two elements of the Silt Array (data from Jana and Stuedlein 2021).**

## References

Jana, A., and A.W. Stuedlein. 2021. "Dynamic In-Situ Response of a Deep, Medium Dense Sand Deposit Deposit." *J. Geotech. Geoenviron. Eng.* 147(6), 04021039.